





Cyclic Zoom: Multi-scale GRMHD Modeling of Black Hole Accretion and Feedback

MINGHAO GUO (郭明浩) ¹, JAMES M. STONE ^{1,2}, ELIOT QUATAERT ¹ AND VOLKER SPRINGEL ³

¹*Department of Astrophysical Sciences, Princeton University, Princeton, NJ 08544, USA*

²*School of Natural Sciences, Institute for Advanced Study, 1 Einstein Drive, Princeton, NJ 08540, USA*

³*Max-Planck-Institut für Astrophysik, Karl-Schwarzschild-Straße 1, D-85740 Garching bei München, Germany*

ABSTRACT

We present a “cyclic zoom” method to capture the dynamics of accretion flows onto black holes across a vast range of spatial and temporal scales in general relativistic magnetohydrodynamic (GRMHD) simulations. In this method, we cyclically zoom out (derefine) and zoom in (refine) the simulation domain while using a central mask region containing a careful treatment of the coarsened fluid variables to preserve the small-scale physics, particularly the magnetic field dynamics. The method can accelerate GRMHD simulations by $\gtrsim 10^5$ times for problems with large scale separation. We demonstrate the validity of the technique using a series of tests, including spherically symmetric Bondi accretion, the Blandford-Znajek monopole, magnetized turbulent Bondi accretion, accretion of a magnetized rotating torus, and the long-term evolution of an accreting torus about both Schwarzschild and Kerr black holes. As applications, we simulate Bondi and rotating torus accretion onto black holes from galactic scales, covering an extremely large dynamic range. In Bondi accretion, the accretion rate is suppressed relative to the Bondi rate by $\sim (10r_g/r_B)^{1/2}$ with a feedback power of $\sim 0.01\dot{M}c^2$ for vanishing spin, and $\sim 0.1\dot{M}c^2$ for spin $a \approx 0.9$. In the long-term evolution of a rotating torus, the accretion rate decreases with time as $\dot{M} \propto t^{-2}$ on timescales much longer than the viscous timescale, demonstrating that our method can capture not only quasi-steady problems but also secular evolution. Our new method likewise holds significant promise for applications to many other problems that need to cover vast spatial and temporal scales.

Keywords: Accretion (14) — Active galactic nuclei (16) — Astrophysical fluid dynamics (101) — Black holes (162) — Bondi accretion (174) — Supermassive black holes (1663) — Magnetohydrodynamics (1964) — Computational methods (1965) — Magnetohydrodynamical simulations (1966)

1. INTRODUCTION

Supermassive black holes (SMBHs), harbored in the nuclei of almost all galaxies, correlate with properties of their hosts (Magorrian et al. 1998; Ferrarese & Merritt 2000; Gebhardt et al. 2000; Kormendy & Ho 2013). How these black holes accrete gas from the ambient background and feed mass, momentum, and energy back into their environments remain crucial unsolved problems. Accurately modeling feeding and feedback from galactic to event horizon scales is a formidable task; the involved spatial scales span nearly nine orders of mag-

nitude (from mpc to Mpc) and need to be resolved over an extended time period (Gaspari et al. 2020). Due to limits of computational power, special prescriptions (“sub-grid” models) to model accretion flows near the SMBHs and their feedback are widely adopted in galactic and cosmological simulations (e.g., Li & Bryan 2014; Weinberger et al. 2017; Tremmel et al. 2017; Pillepich et al. 2018; Springel et al. 2018; Ni et al. 2022; Su et al. 2023; Koudmani et al. 2024; Ni et al. 2024; Weinberger et al. 2025).

On the other hand, general relativistic magnetohydrodynamic simulations (GRMHD) that resolve event horizon scales (Gammie et al. 2003; Narayan et al. 2012; Porth et al. 2019; White et al. 2020; Narayan et al. 2022; Yang et al. 2021; Chael 2025) often adopt idealized initial conditions, e.g., a torus in hydrodynamic

equilibrium (Fishbone & Moncrief 1976; Kozłowski et al. 1978). Modeling infall and accretion on galactic scales from the Bondi radius (Bondi 1952) or even further out may help to construct a more realistic model of black hole accretion at smaller radii (Yuan & Narayan 2014; Gaspari et al. 2020). Connecting the large and small scales is also critical for developing more physical models of black hole growth and feedback in cosmological simulations that lack the physics or resolution to follow the gas at small radii (Hopkins & Quataert 2010, 2011; Li & Bryan 2014).

Recent years have seen considerable efforts to link these scales in various environments using different techniques, including direct simulations assuming smaller scale separation (e.g., Lalakos et al. 2022; Kaaz et al. 2023; Olivares et al. 2023; Lalakos et al. 2024; Galishnikova et al. 2025), “zoom-in” using nested meshes (e.g., Ressler et al. 2018, 2020; Guo et al. 2023, 2024), “super-Lagrangian” or “hyper-refinement” methods (e.g., Anglés-Alcázar et al. 2021; Hopkins et al. 2024a,b, 2025), or remapping between different simulations (Kaaz et al. 2025).

Simply using GRMHD simulations that resolve horizon scales to compute the feedback from the event horizon to galactic scales is generally infeasible due to the very restrictive timestep constraints which limit the evolutionary time that can be modeled. Recently, Cho et al. (2023, 2024) have introduced a “multi-zone” method that greatly accelerates such calculations while passing information both from large to small scales and vice-versa. Inspired by this work, we have developed a very similar but nevertheless new technique we term the “cyclic zoom” method. In our approach, we cyclically zoom in and zoom out the simulation domain using a carefully designed mask in the inner regions that preserves information about the fluid quantities on small-scales. Moreover, the method evolves the magnetic field within the mask to preserve the divergence-free constraint using inductive electric fields that also preserve information from small scales.

The rest of this article is organized as follows. In Section 2 we describe the numerical method and in particular how we formulate the mask region. In Section 3 we illustrate the validity of the method using a series of tests. In Section 4 we then presents results for Bondi and torus accretion over scales which are simply infeasible to model using traditional approaches on current computational resources. In Section 5, we discuss the implications of our results. Finally, we conclude in Section 6.

Throughout the paper, we define the gravitational radius as $r_g = GM/c^2$ and the gravitational time as

$t_g = r_g/c$ assuming a unit system where $GM = c = 1$. As is customary, Greek indices run through $[t, x, y, z]$ and Roman indices span $[x, y, z]$.

2. METHODOLOGY

We perform GRMHD simulations using *AthenaK* (Stone et al. 2024), a performance portable version of the *Athena++* (Stone et al. 2020) code. *AthenaK* supports a variety of reconstruction methods, Riemann solvers, and integrators for solving the GRMHD equations in a Cartesian Kerr-Schild grid. In our simulations, we adopt the piecewise parabolic spatial reconstruction method (PPM4), the HLLE Riemann solver, and the RK2 time integrator to solve the GRMHD equations. The adaptive mesh refinement (AMR) in *AthenaK* allows us to flexibly achieve a high resolution and good performance over an extremely large dynamic range. We apply the first-order flux correction algorithm (described by Lemaster & Stone 2009) in the rare cases that the higher-order fluxes would lead to negative density or pressure. The code framework, equations we solve, and the algorithms implemented in *AthenaK* are described in detail by a series of previous papers including White et al. (2016), Stone et al. (2020), and Stone et al. (2024).

In the GRMHD module, the conserved variables are $U \in \{\rho u^t, \rho u^t + T^t_t, T^t_i\}$, i.e, coordinate-frame mass density with rest-mass density ρ and the stress-energy tensor, which has components

$$T^{\mu\nu} = (\rho + u + p + b^2) u^\mu u^\nu + \left(p + \frac{b^2}{2}\right) g^{\mu\nu} - b^\mu b^\nu, \quad (1)$$

where u is the fluid-frame internal energy density, $p = (\gamma_{\text{ad}} - 1)u$ is the fluid-frame gas pressure with γ_{ad} the adiabatic index, u^μ is the coordinate-frame four-velocity, $b^2 = b^\mu b_\mu$ with b^μ the fluid-frame magnetic field four-vector, and $g^{\mu\nu}$ is the metric. The primitive variables are $W \in \{\rho, u, \tilde{u}^i\}$ where \tilde{u}^i are normal-frame spatial velocity components, related to the coordinate-frame velocity via $u^i = \tilde{u}^i - \alpha\gamma g^{ti}$, where $\alpha = (-g^{tt})^{-1/2}$ is the lapse and γ is the normal-frame Lorentz factor. The coordinate-frame magnetic field B^i , defined as the time component of the dual of the electromagnetic field tensor $*F^{\mu\nu}$, is subject to the divergence-free (no-monopole) constraint

$$\frac{1}{\sqrt{-g}} \partial_i (\sqrt{-g} B^i) = 0, \quad (2)$$

where $g = \det(g_{\mu\nu})$. This reduces to $\nabla \cdot \mathbf{B} = 0$ if $\sqrt{-g} = 1$, as in the Cartesian Kerr-Schild coordinates we adopt here.

2.1. Cyclic Zoom Method

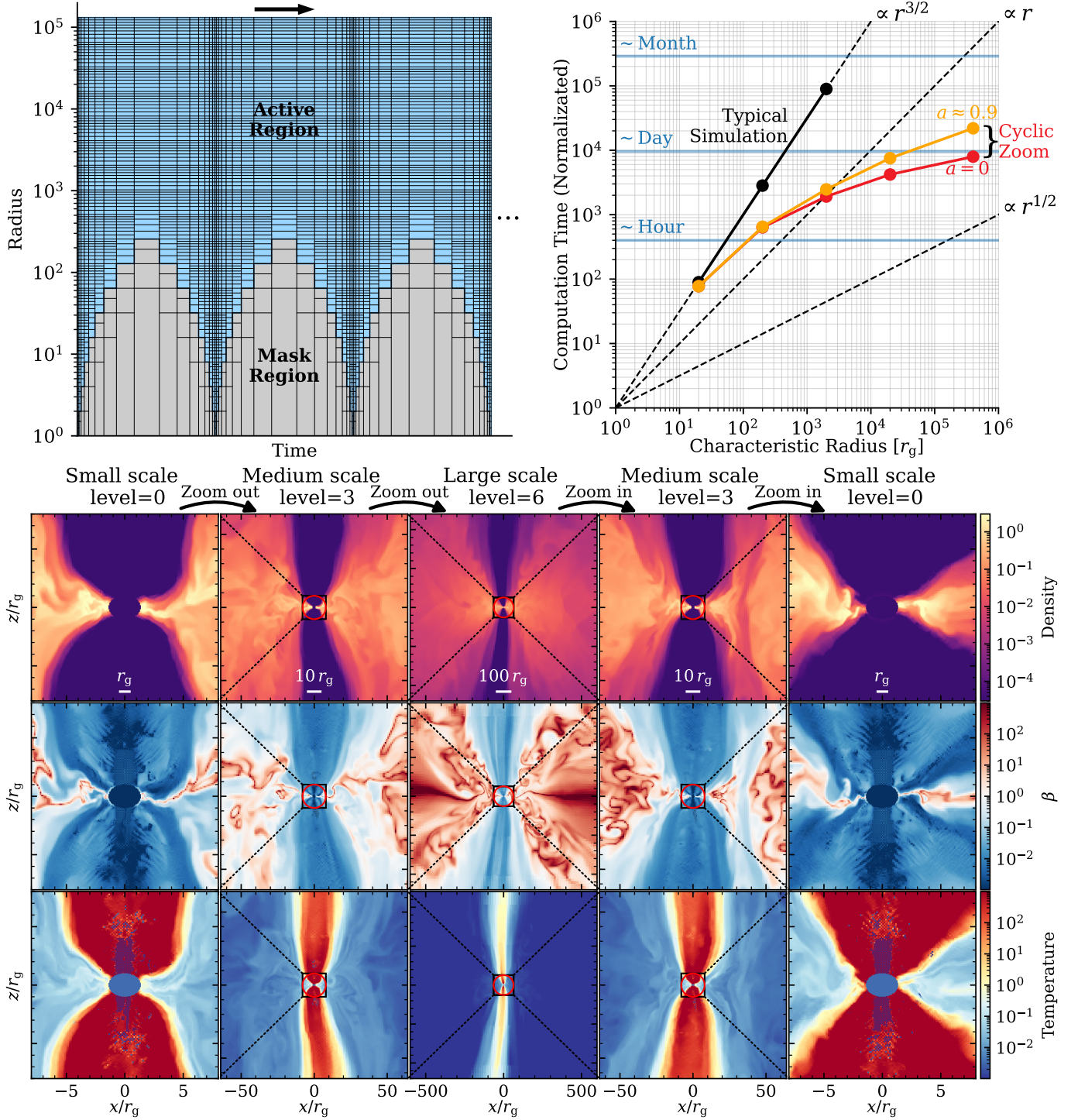


Figure 1. Top left: schematics of the cyclic zoom method in a space-time diagram. Blue marks the active region the gray marks mask region. Runtime is shown along the x -axis (not to scale). The thin lines illustrate the relative spatial resolution and temporal resolution. Here shows three “ Λ -cycles” while a complete simulation typically consists of tens to hundreds of Λ -cycles. Top right: Normalized computation time as a function of characteristic radius (Bondi radius) over one characteristic timescale for Bondi accretion in GRMHD simulations (black dots) and cyclic zoom runs with black hole spin $a = 0$ (red) and $a = 0.9375$ (orange). Blue lines mark typical timescales of an hour, a day, and a month in real-time for one GPU node. Typical simulations follow a scaling of $\propto r^{3/2}$, which quickly becomes prohibitive for growing characteristic radius while the cyclic zoom run is relatively insensitive to the characteristic radius. Bottom: illustration of one Λ -cycle in the cyclic zoom method for accretion of a [Fishbone & Moncrief \(1976\)](#) torus in magnetically arrested state onto a black hole with spin $a = 0.9375$ when the system is quasi-steady. We only show levels $i = 0, 3, 6, 3, 0$ for clarity. The red circles mark the boundary between the mask region in the center and the active region outside. The mask region can maintain the small-scale hydrodynamic and magnetic information and drive the feedback from the central region. It also recovers the accretion flow around the black hole when zooming back into the smallest scale.

The challenge of simulating accretion and feedback from SMBHs to galactic scales is the vast range of spatial and temporal scales. To tackle this problem, we repeatedly zoom out (derefine) and zoom in (refine) the simulation domain, which we denote as the “cyclic zoom” method. The spatial resolution is correspondingly decreased (increased) when we zoom out (in) using AMR to alleviate the timestep constraints while keeping the same relative resolution $\Delta x/x$ for the region of interest. A mask region in the center is used to preserve the small-scale physics. Figure 1 (top left) illustrates the cyclic zoom method in a space-time diagram with relative spatial and temporal resolution. It behaves like a “ Λ -cycle” in the space-time diagram (or “V-cycle”, depending on what we choose as the starting point of the simulation). A complete simulation typically consists of tens to hundreds of Λ -cycles.

The key to the method is the mask region when we do not resolve the event horizon and how we pass information across the boundaries between the mask region and the active region. It is crucial because, without a mask region or any special treatment, the system cannot be aware of small-scale information such as accretion or feedback. In the Cartesian coordinates we use, the mask region (the gray region in Figure 1) is a region of cells within a certain radius $r_{z,i} \equiv 2^i r_g$ for level i , where $i \in \{0, 1, \dots, (n-1)\}$. In the current resolution we use, we resolve the mask region by $r_{z,i} = 16\Delta x_i$, which translates to $\gtrsim 10^4$ cells in the mask region. As we zoom out, it is effectively the boundary of the mask region that prescribes an inner boundary condition for the rest of the domain. At each level, making the mask region larger at fixed Δx resolves the boundary better and in this sense can feed in small scale information more faithfully into the coarser simulation. On the other hand, keeping a fixed mask region is an approximation and not accurate in detail so one may need to avoid using a large volume of mask region. In addition, if the mask region is too large, the timestep will be limited again due to the smaller cell size relative to the active region. So in practice, one should aim for a compromise. After trial and error, we find that a resolution of $r_{z,i}/\Delta x_i \gtrsim 10$ for the mask region is satisfactory. Due to the constraint of computational resources, we have not yet tested a larger size of mask region, which we defer as future work when presenting higher-resolution simulations.

The simulation is simply a standard GRMHD simulation without any additional treatment when $i = 0$. When $i > 0$, to maintain small-scale information, we fix the hydrodynamic variables in the central mask region within $r < r_{z,i}$ at level i to be the coarse-grained hydrodynamic variables from the finer grid at level $i - 1$.

That is, every time step, we reset the primitive hydrodynamic variables W to be a constant W_0 , which is converted from the conservative hydrodynamic variables $U_{\text{hydro}} \in \{\rho u^t, \rho u^t + T_{t,\text{hydro}}^t, T_{i,\text{hydro}}^t\}$ where $T_{\mu,\text{hydro}}^t = (\rho + u + p)u^t u_\mu + p\delta_\mu^t$. Here the coarse-grained conservative hydrodynamic variables are calculated by

$$U_{\text{hydro,coarse}} = \frac{\sum U_{\text{hydro,fine}} \Delta V_{\text{fine}}}{\Delta V_{\text{coarse}}}, \quad (3)$$

where $U_{\text{hydro,fine}}$ is the variables in level $i - 1$ being restricted and ΔV is the volume of the cells on the fine and coarse mesh. We always have $\Delta V_{\text{coarse}} = 8\Delta V_{\text{fine}}$ for the Cartesian mesh we use. In this way, we conserve the hydrodynamic part of the conserved variables.

For the magnetic part, simply holding the magnetic field fixed in the mask region and enforcing the divergence-free constraint may cause a strong shear of the magnetic field lines around the boundary in the presence of rotation and inhomogeneity. Therefore, we still evolve the magnetic field \mathbf{B} according to the induction equation using constrained transport to enforce the divergence-free constraint $\nabla \cdot \mathbf{B} = 0$ as in typical MHD codes. Moreover, to preserve the Poynting flux, we add an extra source term from smaller scales in the mask region, i.e.,

$$\partial_t(\sqrt{-g}\mathbf{B}) + \nabla \times [\sqrt{-g}(\mathcal{E} + \delta\mathcal{E})] = 0. \quad (4)$$

Here $\mathcal{E} = \mathbf{B} \times \mathbf{u}_0$ is the usual electromotive force (EMF) except that the velocity \mathbf{u}_0 in the mask region is fixed. The extra term $\delta\mathcal{E}$ is an additional constant EMF defined along the cell edges, the same way as the edge-centered EMF in *AthenaK* and *Athena++* (Stone et al. 2020). Instead of any ad-hoc models, it is calculated along each direction by

$$\delta\mathcal{E} = \hat{\mathcal{E}}_0 - \mathcal{E}_0, \quad (5)$$

where

$$\hat{\mathcal{E}}_0 = \frac{\sum \mathcal{E}_{\text{fine}} \Delta L_{\text{fine}}}{\Delta L_{\text{coarse}}}, \quad (6)$$

is the average of the edge-centered EMF from the previous finer level right before the mesh derefinement and \mathcal{E}_0 is the EMF computed right after the mesh derefinement. Here ΔL is the length of the cell edges and we always have $\Delta L_{\text{coarse}} = 2\Delta L_{\text{fine}}$ in the Cartesian grid we use. The extra source term is thus the difference between the coarse-grained EMF from the finer variables and the EMF from the coarse-grained variables. In addition, we limit the source term such that $|\delta\mathcal{E}| \leq C \max(\mathcal{E}_0)$ in the mask region to keep the stability of the simulation. Here the prefactor of upper limit C is typically set to be

$C = 1$. The source term vanishes if the fluid is uniform. We find that inclusion of $\delta\mathcal{E}$ is important for preserving the outgoing Poynting flux in the case of rotating black holes.

The conserved variables inside the mask region are thus computed using the fixed primitive variables W_0 and the evolved magnetic field \mathbf{B} correspondingly instead of evolving according to the GRMHD equations. This means that the code is no longer conservative to machine precision in the mask region. But this is expected since the code effectively “skips” evolution of the fluid within r_z . We have numerically verified that the mass change due to this algorithm is approximately equal to that in an analogous normal GRMHD run. The relative difference is $\lesssim 1\%$ (see Appendix A for details).

Correspondingly, when we zoom in from level $i + 1$ to level i with mesh refinement, we perform prolongation for the evolved coarse variables outside the old mask region ($r > r_{z,i+1}$). But for variables within the old mask region ($r < r_{z,i+1}$), since the hydrodynamic variables are not evolved and remain unchanged, we set the primitive variables to be the previously stored finer primitive variables on level i as the best guess instead of prolongation. This will inevitably bring the two states from different physical times into contact at the old mask region boundary ($r_{z,i+1}$), which would cause discontinuities if the system is inhomogeneous. But using anything else will invariably lose crucial information about the small scales, and thus introduce extra errors larger than the current implementation. We still perform prolongation for the magnetic field within the mask region since it is evolved. Then for variables within the new mask region ($r < r_{z,i}$), we still keep the primitive variables fixed during this level. Though not presented in this work, if we start the simulation using the “V-cycle”, we will fill the mask region with pre-defined initial conditions (e.g., a “vacuum sink”, a uniform medium, or a Bondi solution) in the first half cycle.

Finally, the runtime at each level i is typically set by

$$t_{\text{run},i} = f t_{z,i}, \quad (7)$$

where $t_{z,i}$ is the characteristic timescale at $r_{z,i}$ which is defined more precisely below for each problem we study depending on the characteristic speed at $r_{z,i}$. The parameter f is a factor of $\sim O(10)$ to $\sim O(100)$ such that the runtime is sufficient for communication of information between scales. We have verified that the results do not change significantly as long as f is within this range. We typically skip the initial few levels $i = 1$ and $i = 2$ to avoid strong GR effects around the boundary of the mask region, which otherwise would make the mass and energy flux from the horizon preserved in the mask re-

gion less accurate. We shall list the values of the parameters for each run below. where $t_{z,i}$ is the characteristic timescale at $r_{z,i}$ which is defined more precisely below for each problem we study. The parameter f is a factor of $\sim O(10)$ to $\sim O(100)$ such that the runtime is sufficient for communication of information between scales. We have verified that the results do not change significantly as long as f is within this range. We typically skip the initial few levels $i = 1$ and $i = 2$ to avoid strong GR effects around the boundary of the mask region, which otherwise would make the mass and energy flux from the horizon scale that is preserved in the mask region less accurate. At level $i = 1, 2$, we are still partially resolving the horizon with $r_g/\Delta x = 8, 4$, respectively. Then the solution is a combination of the poorly resolved horizon rotation around the ergosphere and the extra source term, which may easily be biased. Therefore, we prefer that the horizon is either completely well resolved or not resolved at all. The downside of this approach is that we have to ensure that the runtime at $i = 0$ is long enough so that the solution converges within $8 r_g$ or further. We shall list the values of runtime parameters for each run below.

As an illustration of the cyclic zoom method in an actual simulation, Figure 1 (bottom) shows an example of Λ -cycle for accretion of a Fishbone-Moncrief (FM; Fishbone & Moncrief 1976) torus in magnetically arrested state onto a black hole with spin $a = 0.9375$ when the system is quasi-steady. The mask region can keep the small-scale structure and provide correct feedback from the central region. We will present a detailed analysis for the torus accretion in Section 3.4.

We note that the goal of the cyclic zoom approach is to obtain statistically equivalent outcomes when turbulent situations are considered, with qualitatively similar flow features. Identical outcomes are of course not obtained and are usually also not needed. In fact, even the conventional fluid simulations involving turbulence can show different outcomes after a long duration due to floating point roundoff errors if we rerun it.

The speedup of the method is shown by the computation time plot in Figure 1 (top right) measured for the case of magnetized Bondi accretion onto a black hole (see Section 3.3 and Section 4.1 for details of the simulation setup). Typical GRMHD simulations follow a scaling of $\propto r^{3/2}$, which quickly becomes prohibitive for growing characteristic radius (Bondi radius for Bondi accretion). Note that this is difficult to accelerate by increasing computational resources (number of CPUs/GPUs), but limited by the timestep constraints. Instead, cyclic zoom runs are relatively insensitive to the characteristic radius. Therefore this method can accelerate the GRMHD

simulations by a factor of $\sim 10^5$ or more when the characteristic radius is large ($\sim 10^6 r_g$). We will discuss the details of speedup in Section 5.2.

In summary, the cyclic zoom framework effectively uses the mask region as a “sub-grid” model. However, instead of ad-hoc analytic or semi-analytic assumptions of the sub-grid model, we use the information directly from a full GRMHD simulation to provide the “inner boundary”. The cyclic zoom method can be thought of as an analog of AMR in time-space, i.e., “Adaptive Time Refinement” (not to be confused with adaptive time stepping, which updates different cells with different frequencies according to the Courant constraint). It can also be viewed as sampling the small-scale physics in the space-time.

2.2. Diagnostics

Following previous GRMHD simulations, we describe the diagnostics used in this work. The relevant diagnostics include mass flux, magnetic field flux, energy flux, and angular momentum flux,

$$\dot{M} \equiv - \int_S \rho u^r \sqrt{-g} d\Omega, \quad (8)$$

$$\Phi_{\text{BH}} \equiv \sqrt{\pi} \int_S |B^r| \sqrt{-g} d\Omega, \quad (9)$$

$$\dot{E} \equiv \int_S T^r_t \sqrt{-g} d\Omega, \quad (10)$$

$$\dot{L} \equiv \int_S T^r_\phi \sqrt{-g} d\Omega, \quad (11)$$

where S is the area, $T^r_t = (\rho + u + p + b^2)u^r u_t - b^r b_t$, and $T^r_\phi = (\rho + u + p + b^2)u^r u_\phi - b^r b_\phi$. Sometimes it is useful to separate the mass flux into inflow and outflow

$$\dot{M} = - \underbrace{\int_{u^r < 0} \rho u^r \sqrt{-g} d\Omega}_{\dot{M}_{\text{in}}} - \underbrace{\int_{u^r > 0} \rho u^r \sqrt{-g} d\Omega}_{\dot{M}_{\text{out}}}. \quad (12)$$

The dimensionless magnetic flux parameter is defined by

$$\phi_{\text{BH}} \equiv \frac{\Phi_{\text{BH}}}{\sqrt{\dot{M}}}. \quad (13)$$

The energy flux \dot{E} includes the flux of rest mass energy, so the “feedback” energy flux is $\dot{M} - \dot{E}$. The efficiency of feedback can thus be defined by

$$\eta \equiv \frac{\dot{M} - \dot{E}}{\dot{M}}. \quad (14)$$

The efficiency is positive (negative) when energy is transported outward (inward). We can further separate the feedback power into the hydrodynamic part

$$\dot{E}_{\text{hydro}} = - \int_S [(\rho + u + p)u^r u_t + \rho u^r] \sqrt{-g} d\Omega, \quad (15)$$

and the electromagnetic (EM) part

$$\dot{E}_{\text{EM}} = - \int_S (b^2 u^r u_t - b^r b_t) \sqrt{-g} d\Omega, \quad (16)$$

Finally, the specific angular momentum flux is defined by $l \equiv \dot{L}/\dot{M}$.

3. VALIDATION

In this section, we present a set of validation simulations. First, we perform tests on problems with known analytic solutions including spherically symmetric Bondi accretion and black hole energy extraction with monopole magnetic field. Then we test problems without known analytic solutions, including magnetized Bondi accretion, torus accretion, and long-term secular evolution of tori. These problems are ideal testbeds for our method. For each case, we compare two runs: a “standard” run, i.e., a standard GRMHD simulation, and a “cyclic zoom” run using the cyclic zoom method we described above. All runs in this section use a sufficiently large cubic box of size $[-2^{17}, 2^{17}]^3 \approx [-1.3 \times 10^5, 1.3 \times 10^5]^3 r_g^3$ with a root grid of 128^3 cells and 15 levels of mesh refinement with the finest resolution of $\Delta x_{\text{min}} = 1/16 r_g$ except for the monopole test which only covers the domain of $z > 0$. The main parameters of these runs are summarized in Table 1. Below we discuss the details of each test.

3.1. Hydrodynamic Bondi Accretion

Spherically symmetric, adiabatic Bondi accretion onto a Schwarzschild black hole (Michel 1972) is a common test problem for GR hydrodynamics codes. Similar to Stone et al. (2024), we set the initial conditions using the solution in Hawley et al. (1984). We use an adiabatic index of $\gamma_{\text{ad}} = 5/3$, and adiabat $K = p/\rho^{\gamma_{\text{ad}}} = 1$, and a sonic point radius $r_c = 16 r_g$ (the same as Cho et al. 2024), corresponding to a Bondi radius $r_B = 2GM/c_{s,\infty}^2 = 2GM/(\gamma_{\text{ad}} T_\infty) \approx 800 r_g^1$ and thus a Bondi time $t_B = r_B/c_{s,\infty} \approx 1.5 \times 10^4 t_g$. We use a cubic box of size $[-2^{17}, 2^{17}]^3 \approx [-1.3 \times 10^5, 1.3 \times 10^5]^3 r_g^3$ with a root grid of 128^3 cells and 15 levels of mesh refinement with a finest resolution of $\Delta x_{\text{min}} = 1/16 r_g$. The outer boundary conditions are prescribed through the analytic solution. The inner boundary is the excision region detailed in Stone et al. (2020). For the cyclic zoom, we set

¹ Some literature defines the Bondi radius to be $r_B = GM/c_{s,\infty}^2$, i.e., half of the Bondi radius defined here.

Table 1. List of standard, validation, and application runs and their main parameters in this work.

Run Type	Model Type	Spin a	r_B (r_g)	β	r_{in} (r_g)	r_{out} (r_g)	r_{peak} (r_g)	γ_{ad}	Half Box Size (r_g)	AMR Level	Runtime t_{run} (t_g)
Standard / Validation (§3)	Hydro Bondi (§3.1)	0	≈ 800					5/3	$2^{17} \approx 10^5$	15	$10^5 (\approx 6t_B)$
	Monopole (§3.2)	0						4/3	$2^{14} \approx 10^4$	12	4×10^3
	MHD Bondi (§3.3)	0	500	1				5/3	$2^{17} \approx 10^5$	15	$2 \times 10^5 (\approx 25t_B)$
		0.9375	500	1				5/3	$2^{17} \approx 10^5$	15	$2 \times 10^5 (\approx 25t_B)$
		0	500	10^3				5/3	$2^{17} \approx 10^5$	15	$2 \times 10^5 (\approx 25t_B)$
		0.9375	500	10^3				5/3	$2^{17} \approx 10^5$	15	$2 \times 10^5 (\approx 25t_B)$
	Torus (§3.4)	−0.9375			20	10^4	43.08	13/9	$2^{17} \approx 10^5$	15	10^5
		−0.5			20	10^4	42.75	13/9	$2^{17} \approx 10^5$	15	10^5
		0			20	10^4	42.42	13/9	$2^{17} \approx 10^5$	15	10^5
		0.5			20	10^4	42.14	13/9	$2^{17} \approx 10^5$	15	10^5
		0.9375			20	10^4	41.94	13/9	$2^{17} \approx 10^5$	15	10^5
	Torus (§3.5)	0			20	100	34.49	13/9	$2^{17} \approx 10^5$	15	10^6
		0.9375			20	100	34.23	13/9	$2^{17} \approx 10^5$	15	2×10^5
Application (§4)	MHD Bondi (§4.1)	0	2×10^4	1				5/3	$2^{20} \approx 10^6$	18	$3 \times 10^7 (\approx 15t_B)$
		0.9375	2×10^4	1				5/3	$2^{20} \approx 10^6$	18	$3 \times 10^7 (\approx 15t_B)$
		0	4×10^5	1				5/3	$2^{24} \approx 10^7$	22	$10^9 (\approx 5t_B)$
		0.9375	4×10^5	1				5/3	$2^{24} \approx 10^7$	22	$10^9 (\approx 5t_B)$
	Torus (§4.2)	0.9375			10^3	10^4	1820	13/9	$2^{24} \approx 10^7$	22	10^7
	Torus (§4.3)	0			20	100	34.49	13/9	$2^{17} \approx 10^5$	15	10^7

NOTE—The validation and the standard runs are performed with the same spatial resolution over the same time duration. All runs are performed with the finest resolution of $\Delta x_{min} = r_g/16$ and the relative resolution on a grid of 128^3 cells per refinement level except for the monopole test which only covers the domain of $z > 0$ using $128 \times 128 \times 64$ cells per level. The number of AMR levels is adjusted according to the box size.

$n = 8$ and

$$t_{run,i} = \begin{cases} 100 t_g & \text{if } i = 0, \\ 0 & \text{if } i = 1, 2, \\ 10 t_{z,i} & \text{otherwise,} \end{cases} \quad (17)$$

where the local dynamical time $t_{z,i} = r_{z,i}/\sqrt{GM/r_{z,i}}$. We run the simulation to $10^5 t_g \approx 6 t_B$, and its main parameters are summarized in Table 1.

Figure 2 (left panel) shows the $z = 0$ density slice at the end of the simulation. Despite the Cartesian grid and multiple times of mesh refinements and derefinements, the solution maintains nearly perfect symmetry. The radial profile of the accretion rate averaged in time over the later half of the simulation is shown in the right panel of Figure 2. The accretion rate is nearly constant

over the whole simulation domain. It is consistent with the predicted Bondi accretion rate within $\lesssim 0.1\%$. This proves that the cyclic zoom method can recover the analytic solution with high precision.

3.2. Blandford-Znajek Monopole

The Blandford & Znajek (1977) (BZ) monopole test problem is another common test problem for GRMHD codes. Following Chael (2024) and Stone et al. (2024), a monopole magnetic field $B^r \propto 1/r^2$ (initialized using a toroidal vector potential) threads a spherically symmetric medium about a Kerr black hole with spin $a = 0.5$. A density power-law $\rho(r) = B^2/\sigma_c \propto r^{-4}$ with $\sigma_c = 10$ is prescribed for the medium. The initial pressure is set to $p = \rho T$ where $T = \gamma_{ad} - 1$ with an adiabatic index $\gamma_{ad} = 4/3$. A ceiling of magnetization $\sigma_{max} = 10$ is applied for stability. We use a box of $x/r_g \in [-2^{14}, 2^{14}]$,

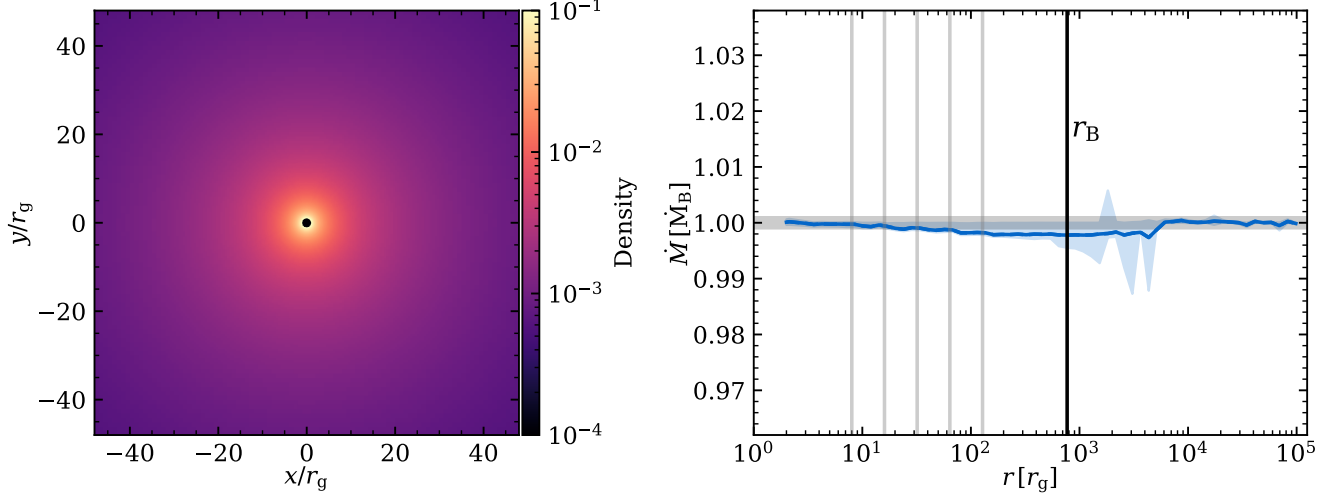


Figure 2. Left: Logarithmic mid-plane density ρ ($z = 0$ slice) from a spherically symmetric Bondi accretion with a Bondi radius of $\sim 800 r_g$ onto a Schwarzschild black hole at the end of the simulation ($t \approx 10^5 t_g \approx 6 t_B$) using the cyclic zoom method. Right: radial profile of time-averaged accretion rate with shaded range showing the 10%-90% time inclusion interval. The vertical black line marks the Bondi radius r_B and the vertical light grey lines mark the boundary of the mask region for all levels. The gray shaded region marks $\pm 0.1\%$ difference from the analytic Bondi accretion rate. The cyclic zoom method maintains the analytic solution within $\sim 0.1\%$ over $\gtrsim 6$ Bondi time.

$y/r_g \in [-2^{14}, 2^{14}]$, $z/r_g \in [0, 2^{14}]$ with a root grid of $128 \times 128 \times 64$ cells and 12 levels of mesh refinement with a finest resolution of $\Delta x_{\min} = 1/16 r_g$. Outflow boundary conditions are applied everywhere except at the $z = 0$ plane, where we instead impose reflecting boundary conditions. For the cyclic zoom run, we set $n = 6$ and

$$t_{\text{run},i} = \begin{cases} 100 t_g & \text{if } i = 0, \\ 0 & \text{if } i = 1, 2, 3, \\ 10 t_{z,i} & \text{otherwise,} \end{cases} \quad (18)$$

where $t_{z,i} = r_{z,i}/c$. We evolve the system for $4 \times 10^3 t_g$. The main parameters are listed in Table 1.

The monopole test challenges the algorithm because the dynamics is governed nearly entirely by the magnetic field. Thus it is a particularly good test of our method for evolving the magnetic field in the mask region. One key diagnostic is the field rotation rate

$$\Omega_F = \frac{b^r u^\phi - b^\phi u^r}{b^r u^t - b^t u^r} \quad (19)$$

after mesh derefinement and refinement. Figure 3 plots the $z = 0$ slice for both the standard and cyclic zoom run. Visual inspection shows that the rotational symmetry is preserved even after $3000 t_g$. More quantitatively, we plot the history of the field rotation rate relative to the horizon rotation rate Ω_H and its time-averaged radial profile. The rotation rate is consistent with the expected solution $\Omega_F/\Omega_H = 1/2$.

In addition, we plot the history and radial profiles of the magnetic flux and the energy flux in Figure 3. The magnetic flux slowly decays due to diffusion with a characteristic timescale of $\sim O(10^3 t_g)$. We find one can improve flux conservation for this test by enforcing the EMF $\mathcal{E}_x = \mathcal{E}_y = 0$ at the $z = 0$ plane. However, we would never be able to use such a fix in any practical applications since it relies on symmetry across the equatorial plane. Even for this monopole test, the initial condition is not perfectly symmetric as there is a net flux of B_z crossing the $z = 0$ plane in the center within the horizon since we initialize the magnetic field using vector potential which prohibits a true monopole inside the simulation domain. The energy feedback efficiency correspondingly decays with time. For the cyclic zoom run, the flux decays slightly more, likely because of the extra diffusion. We confirm this by running a standard run with half of the resolution, which shows decays of magnetic flux and energy flux similar to the cyclic zoom run. Therefore the extra decay is induced by the relatively poor resolution, not the cyclic zoom method itself. Still, the cyclic zoom run is consistent with the standard run within a factor of ~ 2 over thousands of dynamical times (the light-crossing times) in the inner region. The issue of magnetic field decay will be alleviated in the accretion problem where plasma inflow helps to hold the magnetic flux at the horizon, as we shall see in the following tests.

3.3. Magnetized Bondi Accretion

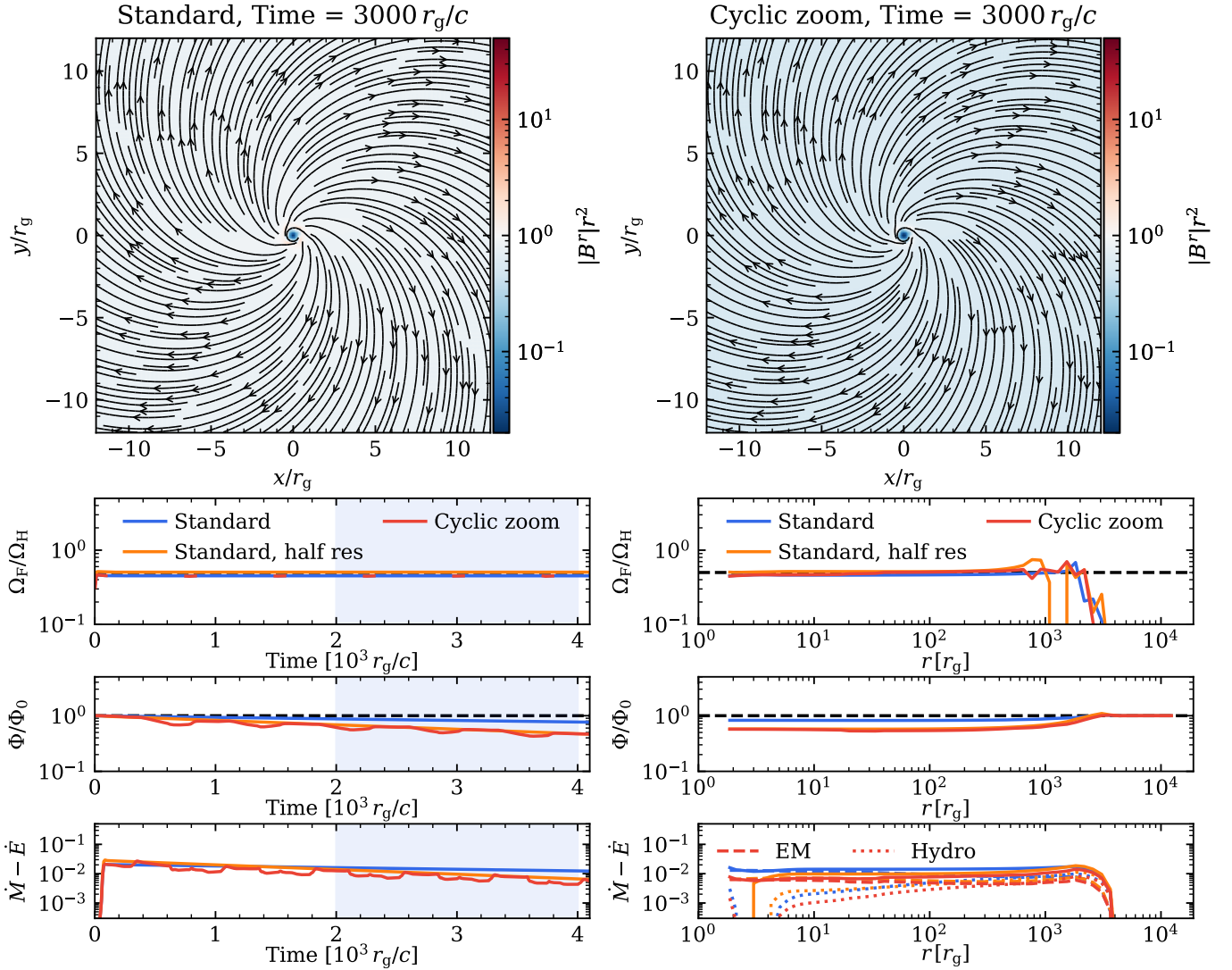


Figure 3. Top: The $z = 0$ slice of magnetic field flux $|B^r|r^2$ with the magnetic field lines from a monopole around a Kerr black hole with $a = 0.5$ in a standard run (left) and a cyclic zoom run (right). The rotational symmetry is preserved even after $3000 t_g$ in the cyclic zoom run. Bottom left: history of field rotation rate measured at the horizon, the magnetic flux at $r = 48 r_g$ and feedback power at $r = 48 r_g$ for the standard run, the cyclic zoom run, and a standard run with half of the resolution everywhere. We average values over the second half of the simulations (blue background) for time-averaged properties. The field rotation rate is recovered accurately. The magnetic flux and feedback power are roughly constant with slow decay, similar to the standard run with half resolution. Bottom right: radial profile of time-averaged field rotation rate, magnetic flux, and feedback power. The cyclic zoom method can reproduce the field rotation rate and the energy flux.

We here model magnetized Bondi accretion onto black holes following a series of previous studies (Lalakos et al. 2022; Cho et al. 2023, 2024; Galishnikova et al. 2025). This problem has no known analytical solution and requires numerical simulations. In the presence of strong magnetic fields, the accretion flow becomes turbulent. Therefore it is a good test problem for our technique.

As an initial condition, instead of the analytic Bondi solution, we specify a uniform background with constant density ρ_∞ and temperature T_∞ , and a constant vertical magnetic field along the z -direction with constant plasma $\beta \equiv p_{\text{gas}}/p_{\text{mag}}$, where $p_{\text{mag}} = b^2/2$. In these

runs, following Galishnikova et al. (2025), we use an adiabatic index $\gamma_{\text{ad}} = 5/3$ and a Bondi radius $r_B = 500 r_g$, and thus a Bondi time $t_B \approx 8 \times 10^3 t_g$. We test spins $a = 0$ and 0.9375 , for $\beta = 1$ and 1000 . The internal energy is perturbed by white noise with a maximum amplitude of 2% to break the symmetry. There are thus four pairs of runs in total, with their main parameters summarized in Table 1.

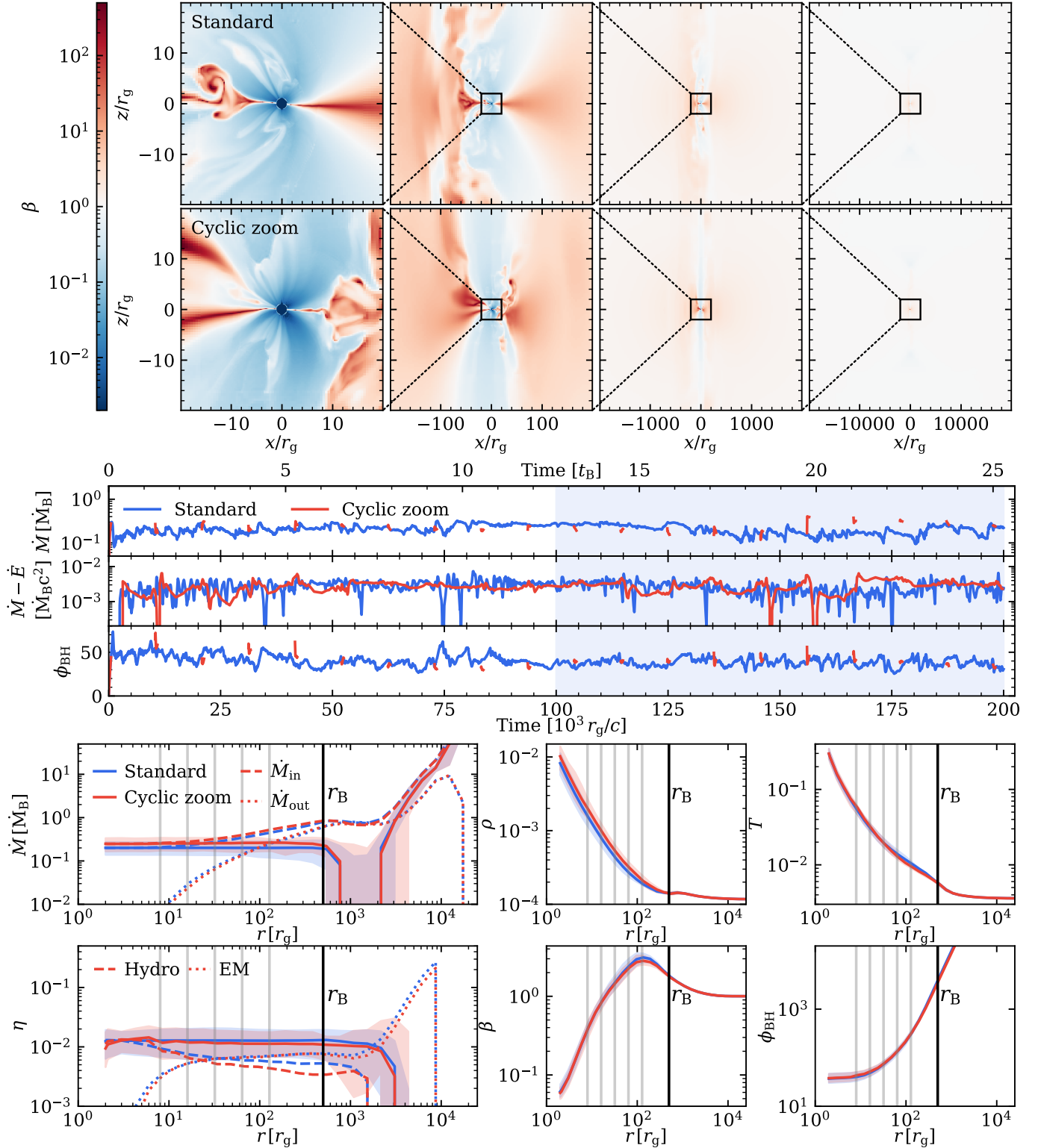


Figure 4. Comparison of the cyclic zoom run with the standard run of Bondi accretion of magnetized plasma with Bondi radius $r_B = 500 r_g$ and initial $\beta = 1$ onto a black hole with spin $a = 0$. Top: the $y = 0$ slice of plasma- β on different scales in the standard run (upper) and the cyclic zoom run (lower) at nearly the end of the simulation. Middle: smoothed history of accretion rate measured at $r = 3 r_g$ normalized by the Bondi accretion rate, energy feedback rate measured at $r = 200 r_g$, and the magnetic flux parameter measured at $r = 3 r_g$. We average values over the second half of the simulations (blue background) for time-averaged properties. Bottom: time-averaged radial profiles of accretion rate with inflow and outflow, density, temperature, feedback efficiency including hydrodynamic part and EM part, plasma- β , and magnetic flux parameter. The vertical black line marks the Bondi radius r_B and the vertical light grey lines mark the boundary of the mask region for all levels. The shaded ranges show the 10%-90% time inclusion interval. The cyclic zoom method captures the evolution, averaged properties, and variability of the accretion flow.

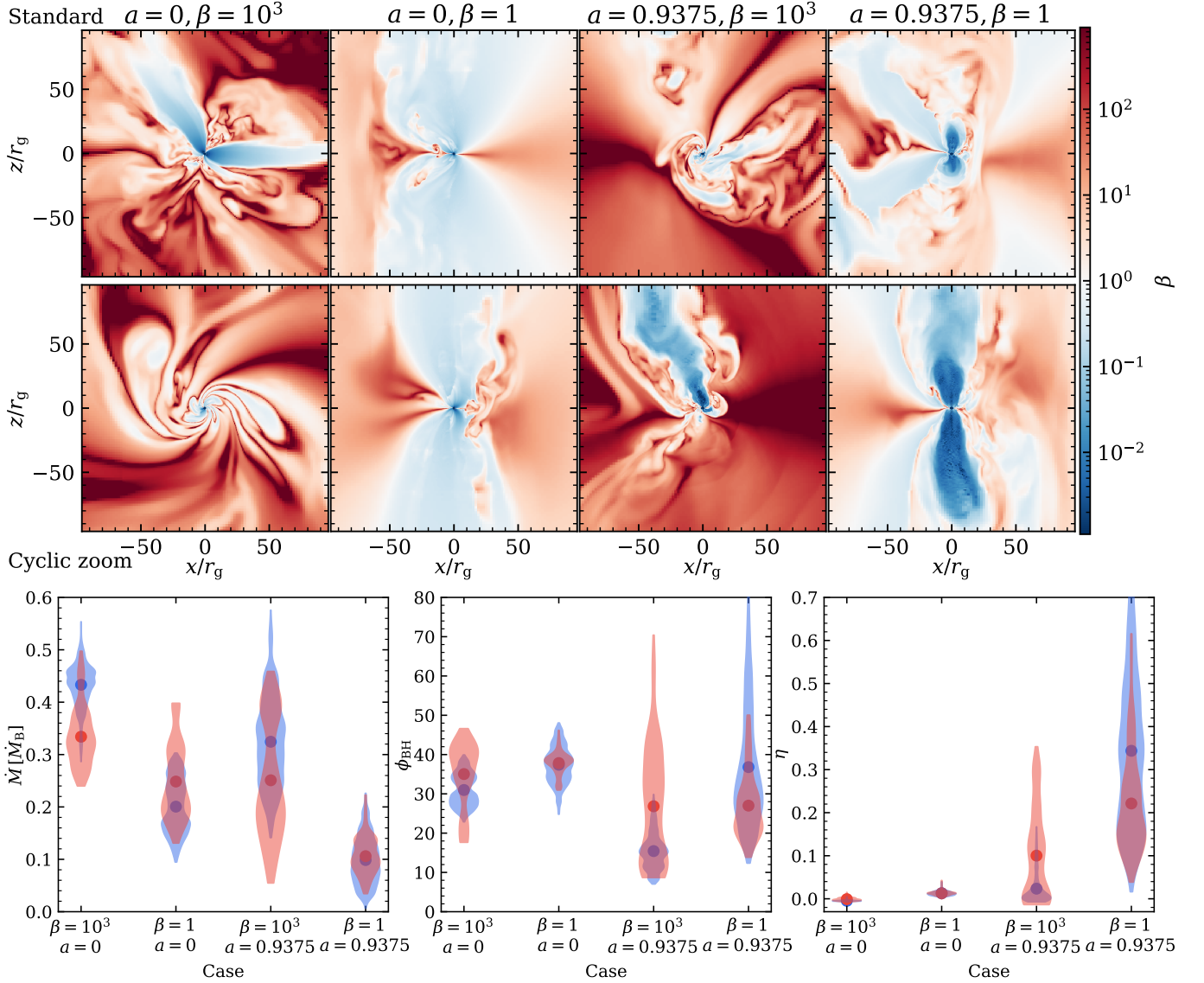


Figure 5. Top: The $y = 0$ slice of plasma- β in the standard runs (top) and the cyclic zoom runs (bottom) in different cases at nearly the end of the simulations. The cyclic zoom runs show similar behaviors to the standard runs. Bottom: distribution of accretion rate (left), magnetic flux parameter (middle), and feedback efficiency (right) of the cyclic zoom method (red) with the standard (blue) runs for Bondi accretion with spin $a = 0, 0.9375$ and plasma- $\beta = 1000, 1$. Compared with the standard runs, the cyclic zoom runs produce similar mean accretion rate, magnetic flux, and feedback efficiency with similar dispersion.

In the cyclic zoom runs, we set $n = 8$ and

$$t_{\text{run},i} = \begin{cases} 500 t_g & \text{if } i = 0, \\ 0 & \text{if } i = 1, 2, \\ \min(50 t_{z,i}, 0.15 t_B) & \text{otherwise.} \end{cases} \quad (20)$$

The runtime at level 0 is $t_{\text{run},i} = 500 t_g$ so that the turbulent fluid and the magnetic field have enough time to relax to a quasi-steady state. The runtime is 50 times the local dynamical time $t_{z,i} = r_{z,i}/\sqrt{GM/r_{z,i}}$ so that the turbulent flow can communicate the information sufficiently. Finally, we cap the runtime at $0.15 t_B$ to capture the variability within the Bondi timescale. In this

way, we reach a speedup of $\gtrsim 10$. All test runs are evolved for $2 \times 10^5 t_g \approx 25 t_B$.

The results for the cases with $a = 0$ and $\beta = 1$ are shown in Figure 4. The accretion flow is turbulent and establishes a quasi-steady state with accretion rate $\dot{M} \sim 0.2 \dot{M}_B$, energy feedback rate $\dot{E} \sim 2 \times 10^{-3} \dot{M}_B c^2$ with efficiency $\eta \approx 1\%$, and saturated magnetic flux of $\phi_{BH} \sim 40$. The upper panel of Figure 4 plots the $y = 0$ slices of plasma- β from small to large scales. The cyclic zoom run reproduces qualitatively similar accretion flows and magnetized outflows. Since the fluid is dynamic and turbulent, we do not expect the system to be in the same state, but look for statistically simi-

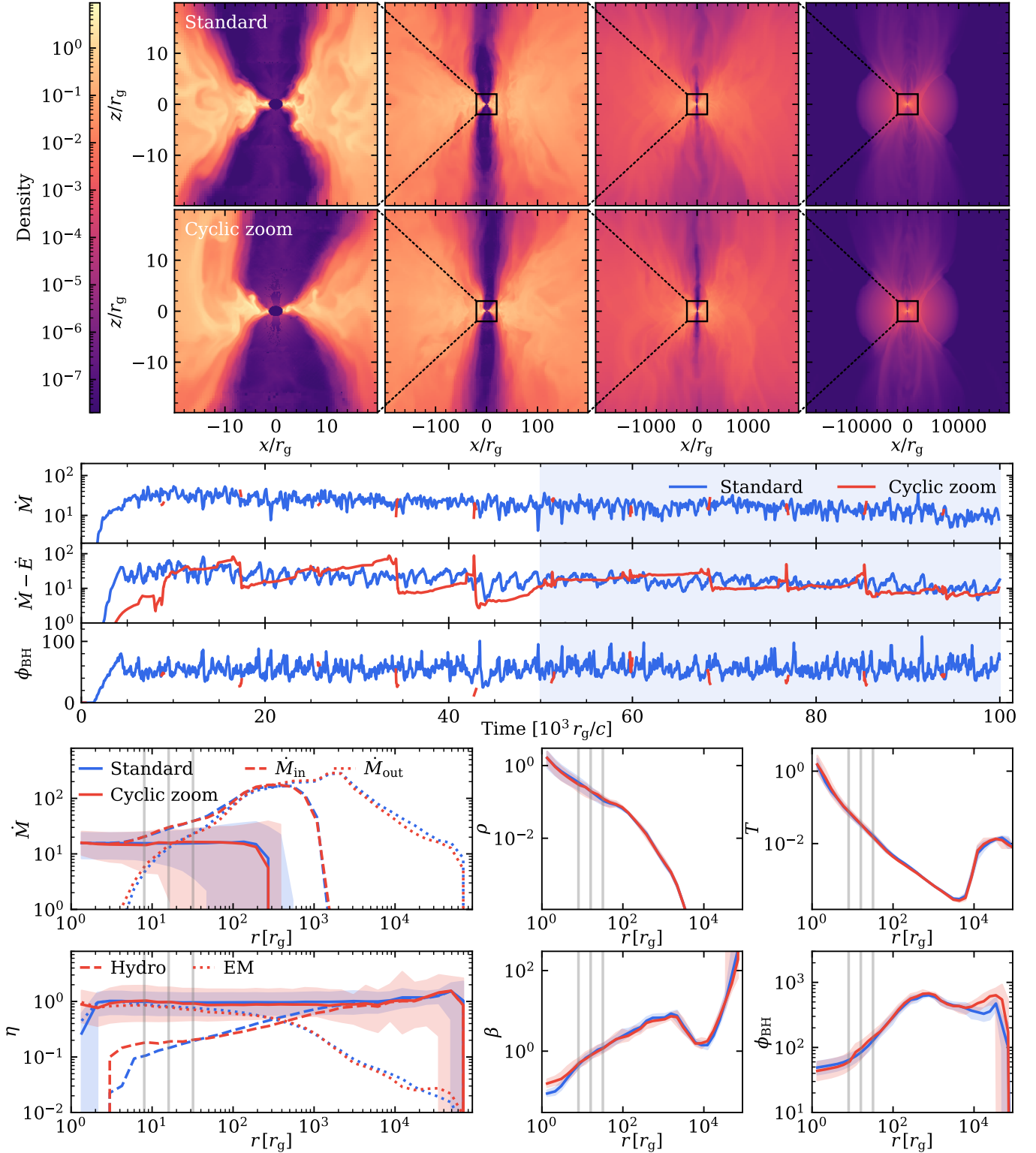


Figure 6. Similar to Figure 4, but for accretion of a FM torus with initial $r_{\text{in}} = 20 r_g$ and $r_{\text{out}} = 10^4 r_g$ onto a spinning black with $a = 0.9375$. The cyclic zoom method can reproduce the feedback efficiency of $\eta \sim 100\%$ shown in the standard run even if the EM part dominates the energy flux.

lar behaviors. In fact, even the standard run can show different snapshots after such a long duration if we re-

run it. From the statistical point of view, the cyclic zoom method captures the mass accretion rate, the en-

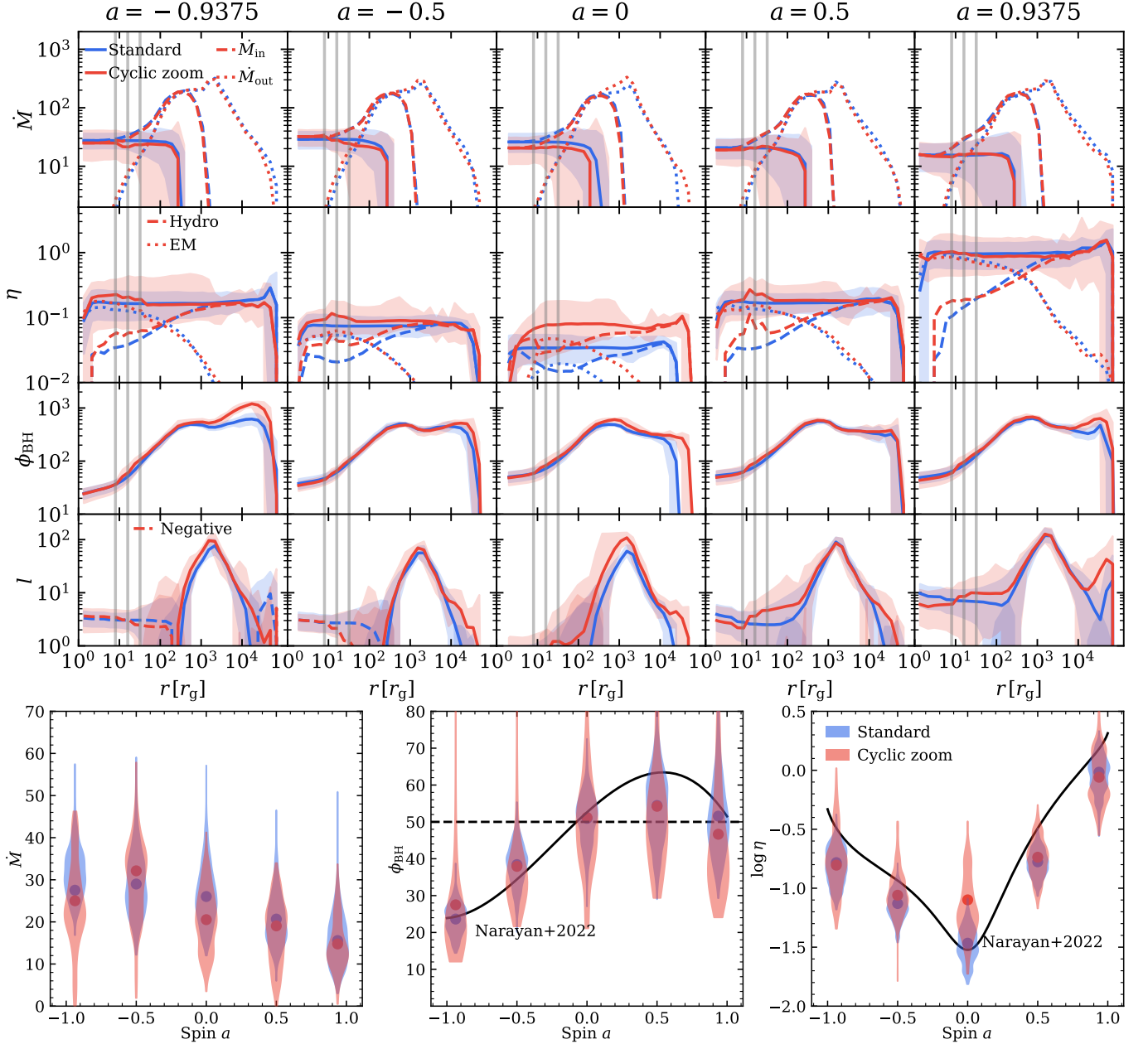


Figure 7. Comparison of the cyclic zoom method (red) with the standard (blue) runs for torus accretion with various spins. Top: time-averaged radial profiles of (from top to bottom) accretion rate, feedback efficiency, magnetic flux parameter, and specific angular momentum flux for different spins. The shaded region shows the 10% – 90% time inclusion interval. The cyclic zoom runs show behaviors similar to those of the standard runs. Bottom left: distribution of accretion rate as a function of spin. Bottom center: distribution of magnetic flux parameter with the black solid line being fit to $\phi_{\text{BH}}(a)$ from Narayan et al. (2022). Bottom right: distribution of feedback efficiency. The black line is the fit from Narayan et al. (2022) plus a constant efficiency of 3% as an estimate of the feedback from the accretion disk itself. The cyclic zoom method can reproduce the results for all spins.

ergy feedback rate, and the magnetic flux parameter very well. As the accretion flow is dynamic and turbulent, we plot the spherically and time averaged radial profiles of the accretion flow in Figure 4. There is excellent consistency between the standard run and the cyclic zoom run. As indicated by the accretion rate, the accre-

tion flow builds a steady state within the Bondi radius through the cyclic zoom method, but the corresponding simulation only costs less than 10% of the computational resources. The variability of the quantities is also similar between the two runs.

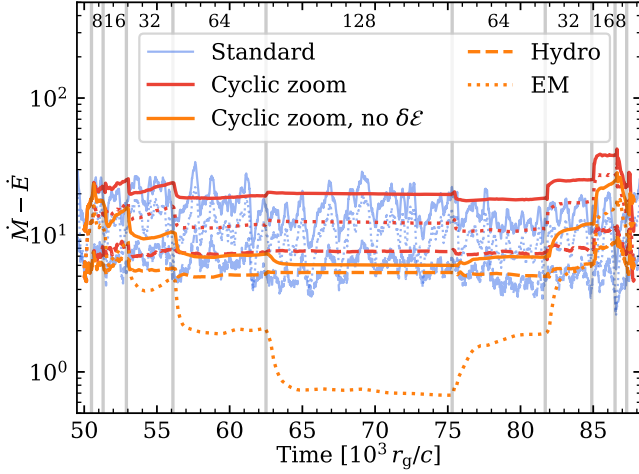


Figure 8. Energy feedback rate measured at $r = 135 r_g$ as a function of time including hydrodynamic and EM part for a FM torus around a black hole with $a = 0.9375$. We show a standard run and two cyclic zoom runs with and without the source term $\delta\mathcal{E}$ in Equation 4. The vertical lines mark the time for zooming out and zooming in with the corresponding $r_{z,i}$. The EM part for the cyclic zoom run without $\delta\mathcal{E}$ decreases by $\sim 30\%$ each time when zooming out. The source term is important in maintaining the outgoing Poynting flux.

The upper panel of Figure 5 plots $y = 0$ slices of plasma- β for all four pairs of runs at nearly the end of the simulations. All the runs show qualitatively similar accretion flows. The lower panel of Figure 5 shows the time-averaged accretion rate \dot{M} , the magnetic flux parameter ϕ_{BH} and the feedback efficiency η , and their distributions in all the four pairs of runs. Overall, the cyclic zoom runs produce very similar results to the standard runs. Note that for $a = 0$ and $\beta = 10^3$ the magnetic field is too weak to produce positive feedback, whereas the case with $a = 0.9375$ and $\beta = 10^3$ has a relatively larger variability, as found by Galishnikova et al. (2025). Thus this run is more challenging to reproduce accurately yet the cyclic zoom method does well.

3.4. Torus Accretion

The accretion of a torus onto a black hole is another standard test problem for GRMHD codes (e.g., Porth et al. 2019). Following Narayan et al. (2022), we perform a suite of simulations of magnetically arrested disks (MAD) with different spins, $a = -0.9375, -0.5, 0, 0.5$, and 0.9375 . We initialize the simulations with the Fishbone & Moncrief (1976) torus solution, which is determined by four parameters: the inner edge of the torus r_{in} , the location of the pressure maximum r_{peak} , the adiabatic index of the fluid γ_{ad} , and the maximum density ρ_{max} . The location of the outer edge of the torus

is a function of these parameters. We set $r_{\text{in}} = 20 r_g$ for all cases and adjust r_{peak} according to a so that $r_{\text{out}} \approx 10^4 r_g$. We adopt an ideal gas equation of state with an adiabatic index of $\gamma_{\text{ad}} = 13/9$.

The magnetic field is initialized with a weak single large magnetic field loop defined by the poloidal vector potential A_ϕ :

$$A_\phi = \max(0, q),$$

$$q = \left[\left(\frac{\rho}{\rho_{\text{max}}} \right) \left(\frac{r}{r_{\text{in}}} \right)^3 e^{-r/r_{\text{mag}}} \sin^3 \theta \right] - A_{\phi, \text{cut}}, \quad (21)$$

where we set $r_{\text{mag}} = 400 r_g$ and $A_{\phi, \text{cut}} = 0.2$. After determining the field components via the vector potential of Equation 21, we normalize the initial magnetic field strength in the disk following Porth et al. (2019) such that the maximum gas pressure and the maximum magnetic pressure in the torus (which do not necessarily occur at the same location) satisfy $\beta_{\text{max}} \equiv (p_{\text{gas}})_{\text{max}} / (p_{\text{mag}})_{\text{max}} = 100$. The internal energy is perturbed by white noise with a maximum amplitude of 2% to break symmetry and excite the magnetorotational instability (MRI) inside the torus.

For the cyclic zoom runs, we set $n = 6$ and the runtime

$$t_{\text{run}, i} = \begin{cases} 500 t_g & \text{if } i = 0, \\ 0 & \text{if } i = 1, 2, \\ 100 t_{z, i} & \text{otherwise,} \end{cases} \quad (22)$$

where $t_{z, i} = r_{z, i} / c$ since the fastest speed on all scales is the speed of light due to the presence of relativistic jets. Each simulation is evolved for $10^5 t_g$ to reach a statistically steady state. In this way, we reach a speedup of ~ 10 . The details of the parameters and runtime are summarized in Table 1.

Figure 6 compares the cyclic zoom run with the standard run for the fast spinning case with $a = 0.9375$. The cyclic zoom run reproduces similar accretion flow, jet, and all the key quantities. It reaches a flat mass flux within $\sim 200 r_g$, similar to the standard runs. The mass outflow profile is also very similar to the standard results, indicating that the large-scale evolution of the torus is also correctly captured. The accretion flow reproduces the strong BZ jet with a similar feedback efficiency of $\sim 100\%$, and similar dispersion ranging from $\sim 60\%$ to $\sim 200\%$. The feedback efficiency profiles are flat within $\sim 10^5 r_g$ similar to the standard run. The system is in a MAD state with the normalized magnetic flux parameter around the horizon $\phi_{\text{BH}} \sim 50$, similar to the standard run.

Time-averaged radial profiles of the accretion rate, magnetic flux parameter, feedback efficiency, and specific angular momentum flux for different spins are

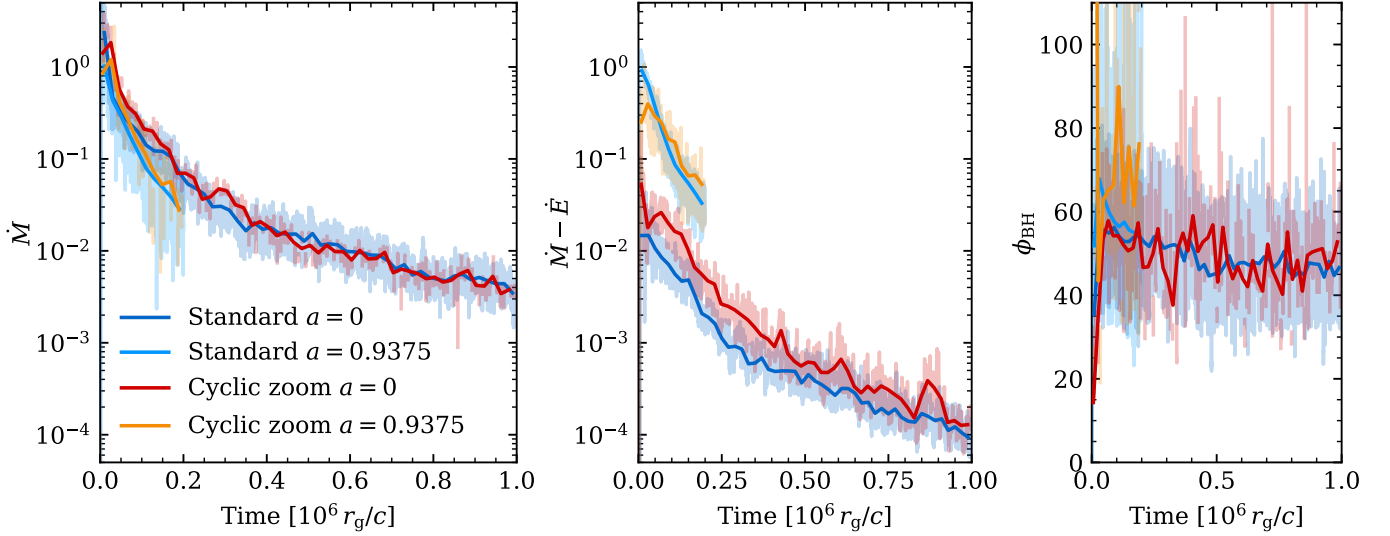


Figure 9. Smoothed history of accretion rate at $r = 3r_g$, feedback energy flux at $r = 200r_g$, and magnetic flux parameter at $r = 3r_g$ for the cyclic zoom method and the standard runs of the long-term evolution of torus accretion with $a = 0$ and $a = 0.9375$. The shaded region shows the variability of the variables. The cyclic zoom method is capable of capturing the secular evolution of the viscous torus over a long time.

shown in Figure 7. The cyclic zoom runs reach a steady state within $\sim 200r_g$ for all spins. The dependence of these variables on spins is correctly captured within $\sim 10\%$ for most cases. The one that is not so satisfying is the case with $a = 0$, where the efficiency is overestimated by a factor of ~ 2 . This is because the Poynting flux is slightly overestimated in the cyclic zoom method. But still, the feedback power is much better than previous works using analytic models as they cannot obtain the accretion rate accurately (e.g., Weinberger et al. 2025).

To demonstrate the dependence of the tests on the BH spin, we further show the distribution of accretion rate, magnetic flux parameter, and feedback efficiency as a function of spin in Figure 7. The accretion rate has a weak dependence on the BH spin. The magnetic flux parameter follows the functional fit from Narayan et al. (2022) (see also Tchekhovskoy et al. 2011; Chael 2025) based on a series of torus accretion simulations. The feedback efficiency also follows the formula fitted by Narayan et al. (2022) plus a constant efficiency of 3% as an estimate of the feedback from the accretion disk itself. Overall, the cyclic zoom method can reproduce the dependence of these quantities on spin.

To highlight that the inclusion of $\delta\mathcal{E}$ is important for preserving the outgoing Poynting flux in the case of rotating black holes, we perform two extra cyclic zoom runs with and without the source term $\delta\mathcal{E}$ in Equation 4. The cyclic zoom runs are restarted from the standard run of the FM torus around a spinning black hole with $a = 0.9375$ at a time when it expands to larger radii and stays in a quasi-steady state ($t = 5 \times 10^4 t_g$). For the

cyclic zoom, we set $n = 8$ and the runtime

$$t_{\text{run},i} = \begin{cases} 500 t_g & \text{if } i = 0, \\ 0 & \text{if } i = 1, 2, \\ 100 t_{z,i} & \text{otherwise,} \end{cases} \quad (23)$$

where $t_{z,i} = r_{z,i}/c$. The history of the feedback power in Figure 8 shows that, without $\delta\mathcal{E}$, the Poynting flux is reduced by $\sim 30\%$ each time we zoom out if the horizon is not resolved. It is ~ 10 times smaller than the standard run when we zoom out to large scales ($r_{z,i} = 128r_g$). The decline of the Poynting flux leads to a smaller feedback power on large scales. On the other hand, the cyclic zoom run that includes the source term from small scales can maintain the Poynting flux even if $r_{z,i}$ is large.

3.5. Long-Term Evolution of Torus Accretion

Apart from the statistically steady states, we also aim to simulate the long-term evolution of accreting systems using the cyclic zoom method, which is computationally not feasible in current GRMHD simulations due to the very long viscous timescale compared with the dynamical timescale, i.e., $t_{\text{visc}} \gtrsim 10^3 t_{\text{dyn}}$. We use a setup similar to Section 3.4 with spin $a = 0$ or 0.9375 , and $r_{\text{in}} = 20r_g$, except that we use a smaller outer radius $r_{\text{out}} = 100r_g$ so that the torus mass is concentrated around $\sim 50r_g$. Such a radially concentrated torus produces significant secular evolution on resolvable timescales. The cyclic zoom parameters are the same as those of the tori studied in Section 3.4.

To study the secular evolution, we run the standard simulations for a very long time of $10^6 t_g$ for the

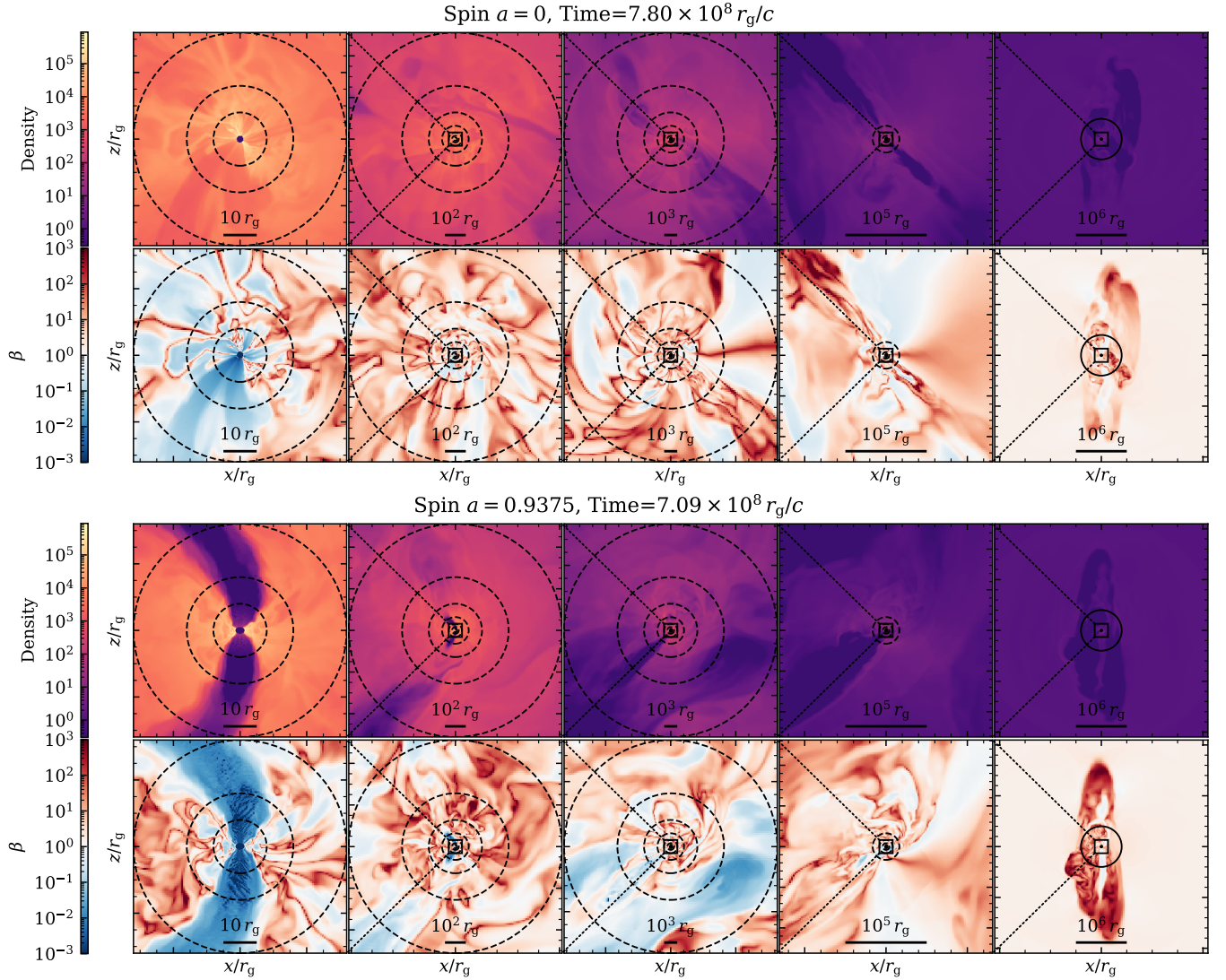


Figure 10. Slice of $y = 0$ plane in Bondi accretion with $r_B = 4 \times 10^5 r_g$ and spin $a = 0$ (top) and $a = 0.9375$ (bottom) using the cyclic zoom method. The dashed circles mark the boundary of each mask region. The solid circle in the rightmost panels marks the Bondi radius. The accretion flow is turbulent on all scales within the Bondi radius. The jet launched by the spinning black hole is typically choked well inside the Bondi radius.

case with $a = 0$, and for $2 \times 10^5 t_g$ for the case with $a = 0.9375$. The history of the accretion rate, the feedback power, and the magnetic flux parameter are shown in Figure 9. The cyclic zoom method can capture the secular evolution of the torus very well over a factor of ~ 100 in accretion rate for $a = 0$. Therefore, apart from steady or statistically steady states, the cyclic zoom method is also suitable for systems undergoing secular evolution. We will further analyze the longer-term dependence and discuss the details of the secular evolution in Section 4.3.

4. APPLICATIONS

In this section, we present our results for a series of problems that are computationally not feasible in the

foreseeable future using standard GRMHD simulations. In particular, we consider Bondi accretion with a large Bondi radius of $4 \times 10^5 r_g$, accretion of a giant torus, and very long-term evolution of a torus.

4.1. Magnetized Bondi Accretion over Galactic Scales

Here we simulate the accretion of magnetized plasma with a Bondi radius $r_B = 4 \times 10^5 r_g$, $\beta = 1$ and spin $a = 0$ and $a = 0.9375$ for about one billion t_g ($\approx 5 t_B$ where $t_B \approx 1.8 \times 10^8 t_g$). The corresponding temperature is $T_\infty \approx 2 \times 10^7$ K, similar to the typical temperature of the hot plasma in elliptical galaxies (Russell et al. 2015). The simulation time translates to ~ 1 Myr for M87*-like SMBHs (Event Horizon Telescope Collaboration et al. 2019). We use a cubic box of size $[-2^{24}, 2^{24}]^3 \approx [-1.7 \times$

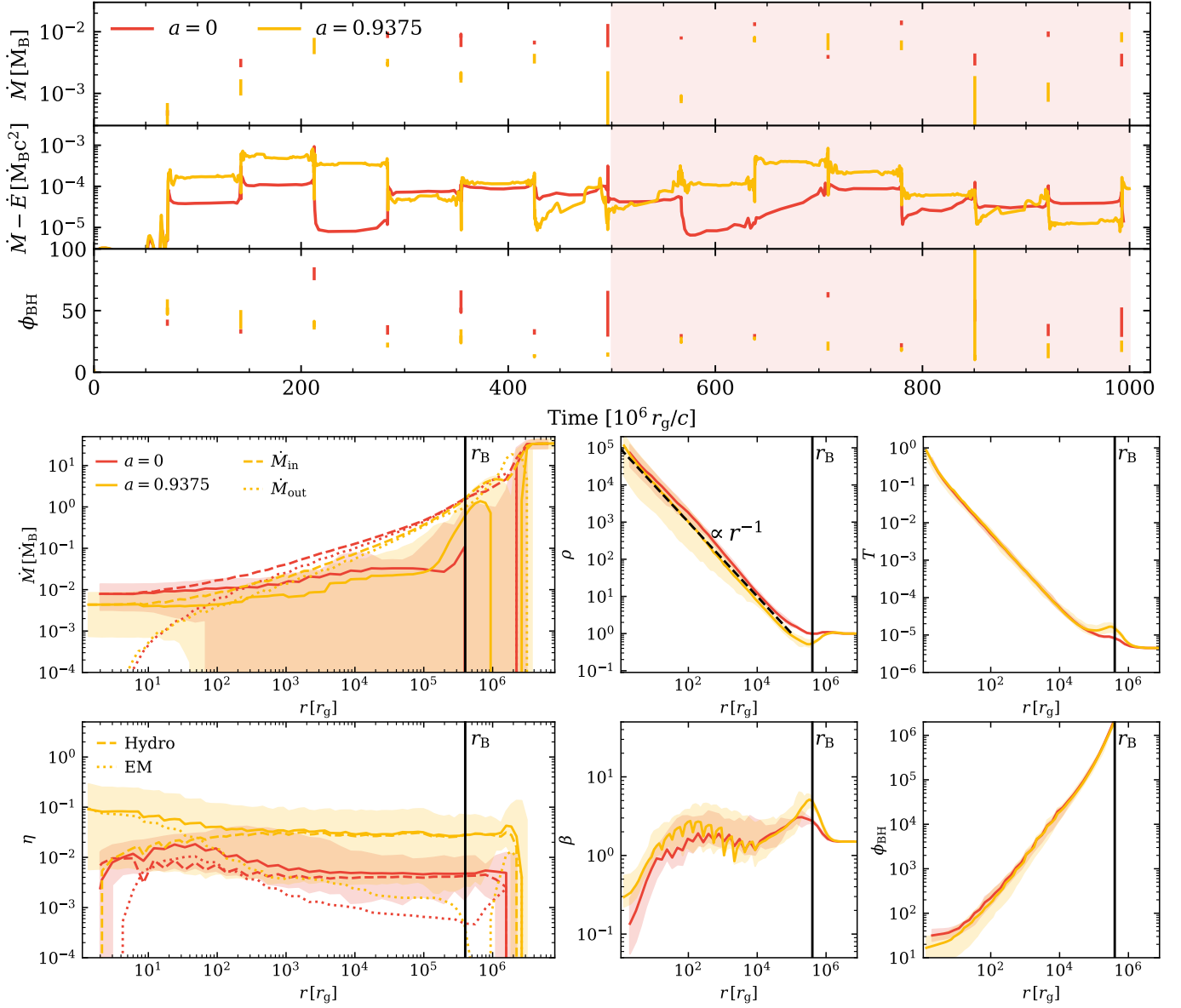


Figure 11. Similar to Figure 4 but for magnetized Bondi accretion with $r_B = 4 \times 10^5 r_g$ and $a = 0$ (red) and $a = 0.9375$ (yellow) using the cyclic zoom method. The history of feedback power is measured at $r \approx 2 \times 10^4 r_g$. The time-averaged accretion rate is $1\% \dot{M}_B$ and the feedback efficiency is $\sim 1\%$ for $a = 0$ and $\sim 10\%$ for $a = 0.9375$. The feedback efficiency has a wide distribution. The density scales with radius as $\rho \propto r^{-1}$.

$10^7, 1.7 \times 10^7]^3 r_g^3$ with a root grid of 128^3 cells and 22 levels of mesh refinement. For the cyclic zoom, we set $n = 15$ and use the runtime

$$t_{\text{run},i} = \begin{cases} 500 t_g & \text{if } i = 0, \\ 0 & \text{if } i = 1, 2, \\ \min(25 t_{z,i}, 0.15 t_B) & \text{otherwise,} \end{cases} \quad (24)$$

where the local dynamical time is $t_{z,i} = r_{z,i} / \sqrt{GM/r_{z,i}}$.

Figure 10 shows slices across the $y = 0$ plane for density and plasma- β , for the cases with $a = 0$ and $a = 0.9375$ at a later stage. The symmetry of Bondi ac-

cretion is clearly broken on all scales within the Bondi radius. We note that the flow structure varies from time to time for both cases, with jets appearing and disappearing. Overall, there is typically stronger feedback for the spinning case. The jets are often “choked” on the mesoscales interior to the Bondi radius. The feedback does not show a preference for a certain direction within the Bondi radius, even for a highly spinning black hole. This indicates that it is hard for the relativistic jets to propagate out to the Bondi radius. Fluid rotation may be required for a persistent jet (Galishnikova et al. 2025).

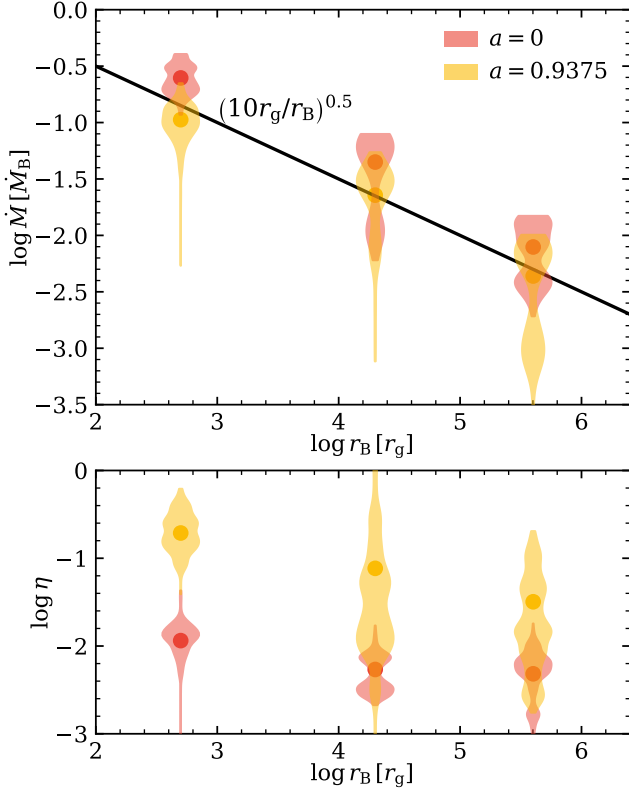


Figure 12. Accretion rate measured at $r = 3 r_g$ and feedback efficiency measured at $r \approx 0.3 r_B$ as a function of Bondi radius for spin $a = 0$ and 0.9375 . Accretion rate scales with Bondi radius as $\dot{M}_{\text{acc}}/\dot{M}_B \approx (10 r_g/r_B)^{1/2}$. The feedback efficiency is roughly $\sim 1\%$ for the Schwarzschild black hole and $\sim 10\%$ for the spinning black hole.

Figure 11 shows the evolution and time-averaged radial profiles of key variables including the accretion rate, the energy feedback rate, and the magnetic flux parameter. The accretion rate is $\sim 1\% \dot{M}_B$ for $a = 0$ and $\sim 0.5\% \dot{M}_B$ for $a = 0.9375$. The net accretion rate is constant within $\sim 10^3 r_g$ but slightly increases going to larger radii. This is partially because of the relatively short time of evolution for the average. In addition, it is very hard to find a flat accretion profile as both the inflow and the outflow are very strong. As a result, the accretion rate exhibits considerable variability, which is higher when the black hole is spinning. The feedback efficiency is $\sim 1\%$ for $a = 0$ and $\sim 10\%$ for $a = 0.9375$. We note that for $a = 0.9375$, the feedback has a noticeably stronger variability with feedback efficiency ranging from $\sim 1\%$ to $\sim 30\%$. For the feedback, we also see a gradual transition from EM energy flux to hydrodynamic energy flux at larger radii. Within the Bondi radius, the mass inflow rate $\dot{M}_{\text{in}} \propto r^{1/2}$ and the density profile follows $\rho \propto r^{-1}$, consistent with the suppression of the net accretion rate. This radial dependence of

the density may be universal, as is reported in various contexts and with varying physics (Ressler et al. 2018, 2020; Xu & Stone 2019; Xu 2023; Guo et al. 2020, 2023, 2024; Lalakos et al. 2022; Cho et al. 2023, 2024). The gas keeps moderately magnetized with the azimuthally averaged plasma- $\beta \sim 1$ at all radii.

The accretion rates and feedback efficiencies for accretion with different Bondi radii found in this work are summarized in Figure 12, including two extra runs with an intermediate Bondi radius of $r_B = 2 \times 10^4 r_g$ (see Table 1). Overall we find a good agreement with a scaling according to $\dot{M}_{\text{acc}}/\dot{M}_B \approx (10 r_g/r_B)^{1/2}$. The feedback efficiency is roughly $\sim 1\%$ for the Schwarzschild black hole and $\sim 10\%$ for the highly spinning black hole. Note that for the spinning black hole, the feedback efficiency has a larger dispersion, reflecting the higher variability in this case, consistent with Galishnikova et al. (2025). We note that a more frequent sampling on small scales may help to better capture this variability.

4.2. Accretion of Torus over Galactic Scales

Here we evolve a more realistic torus initially located between $r_{\text{in}} = 10^3 r_g$ and $r_{\text{out}} = 10^4 r_g$ around a black hole with spin $a = 0.9375$. Correspondingly we set a larger exponential falloff radius for the vector potential of $r_{\text{mag}} = 4000 r_g$. We use a cubic box of size $[-2^{24}, 2^{24}]^3 \approx [-1.7 \times 10^7, 1.7 \times 10^7]^3 r_g^3$ with a root grid of 128^3 cells and 22 levels of mesh refinement. For a cyclic zoom, we set $n = 11$ and use a runtime

$$t_{\text{run},i} = \begin{cases} 500 t_g & \text{if } i = 0, \\ 0 & \text{if } i = 1, 2, \\ 100 t_{z,i} & \text{otherwise,} \end{cases} \quad (25)$$

where $t_{z,i} = r_{z,i}/c$. We evolve the torus for 10 million t_g to reach a statistically steady state.

The evolution of key variables and time-averaged radial profiles of the accretion flow is shown in Figure 13. We reach a quasi-steady state within $\sim 2 \times 10^3 r_g$, as is shown in the radial profile of the accretion rate. Due to the presence of both strong inflow and outflow of the torus, it is hard to get a very flat profile. In addition, the accretion rate may not be necessarily constant since the torus is gradually evolving. The feedback efficiency profile is flat within $\sim 10^7 r_g$ with a mean value of 50% fluctuation between $\sim 10\% - 100\%$. The density profile follows $\rho \propto r^{-1}$ within $10^3 r_g$. The magnetic flux parameter is still $\phi_{\text{BH}} \sim 50$, meaning that the accretion flow is still a MAD. This test challenges the cyclic zoom method's ability to maintain the jet even if the horizon is completely unresolved as the finest resolution becomes $\Delta x = 64 r_g$ when $i = 10$. It also confirms that a giant

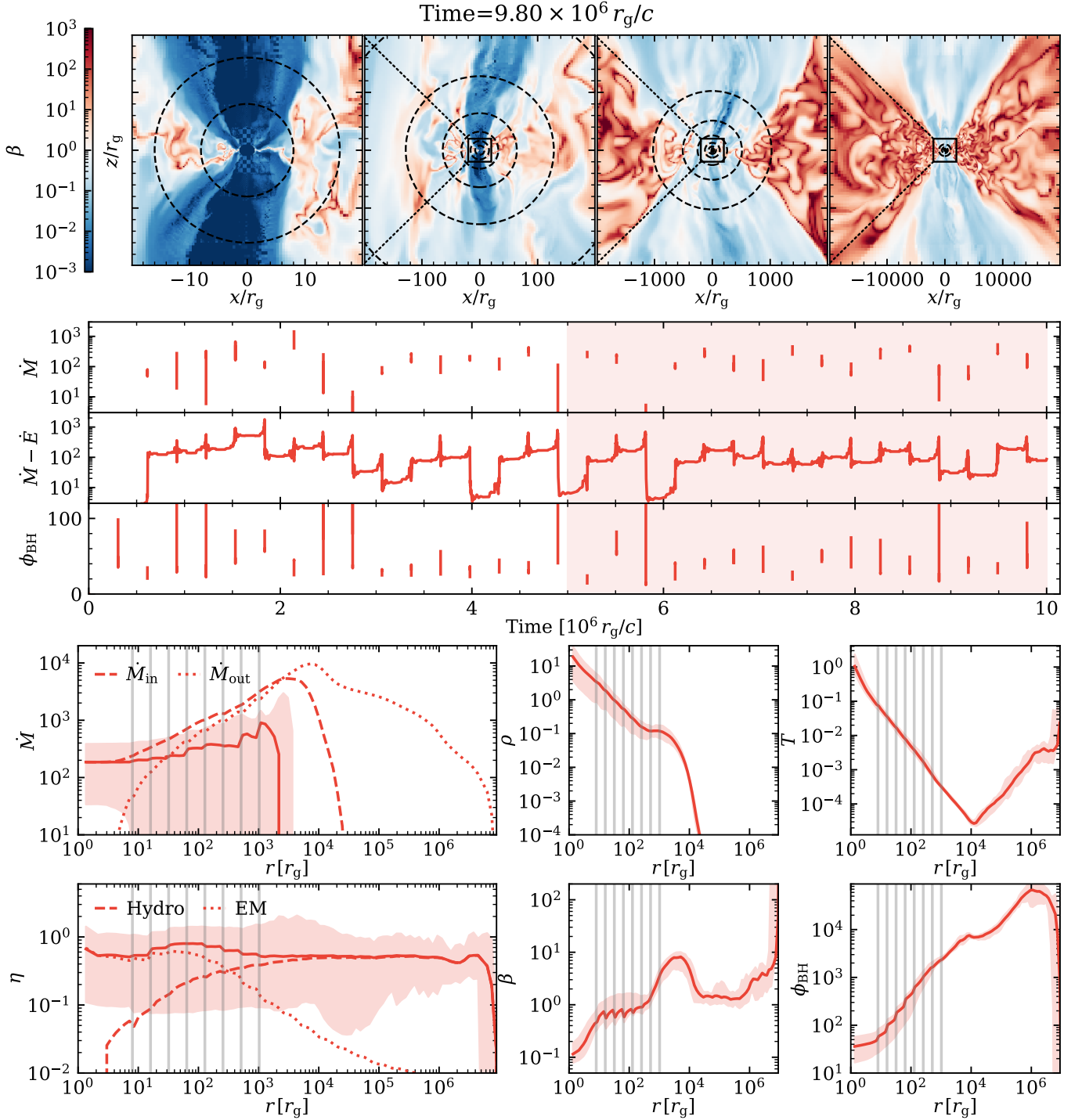


Figure 13. Similar to Figure 4 but for accretion of a large FM torus initially between $r_{\text{in}} = 10^3 r_g$ and $r_{\text{out}} = 10^4 r_g$ onto a spinning black hole with $a = 0.9375$ using the cyclic zoom method. The dashed circles mark the boundary of each mask region. The history of feedback energy flux is measured at $r \approx 10^3 r_g$. We reach a quasi-steady state within $\sim 2 \times 10^3 r_g$ and a constant feedback efficiency within $\sim 10^7 r_g$ with a mean value of 50% fluctuation between $\sim 10\% - 100\%$.

torus located at $\sim 10^3 r_g$ or farther around a spinning black hole is able to produce a strong, sustained jet over a long timescale.

4.3. Long-Term Evolution of Torus Accretion

In this subsection we track the evolution of a torus until almost all of the mass is either accreted onto the black hole or turned into outflows capable of escaping to infinity. We continue running the torus presented

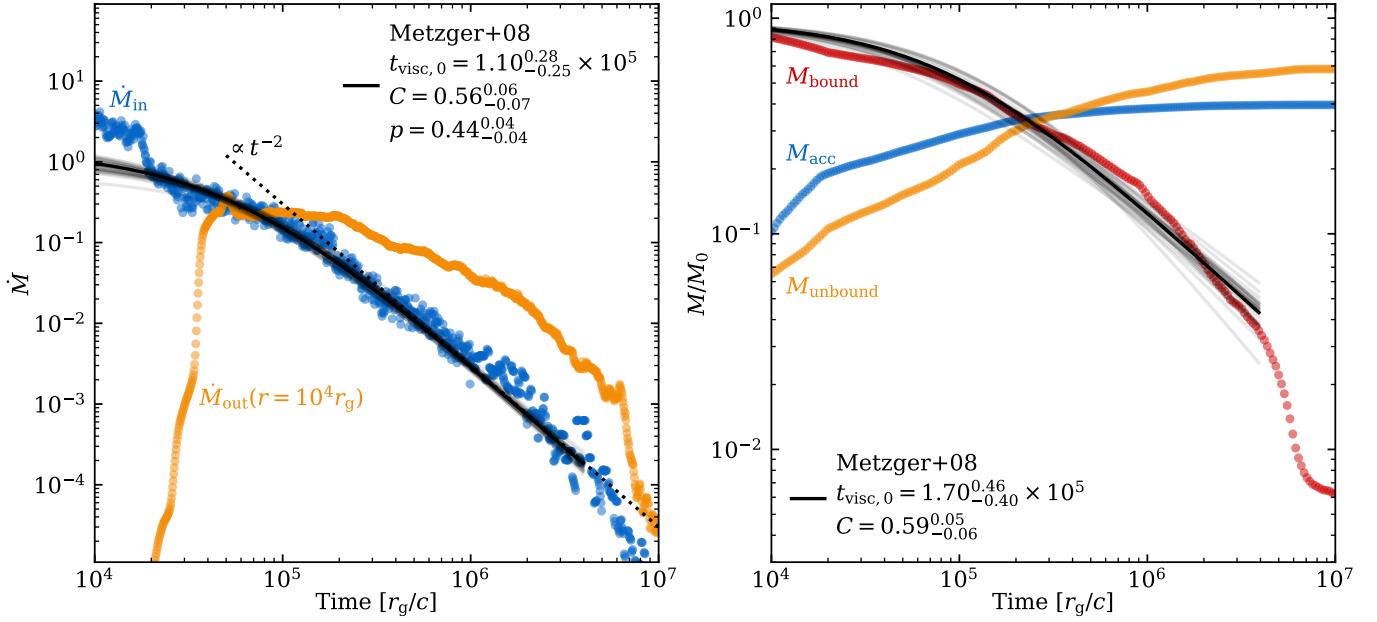


Figure 14. Smoothed long-term evolution of a FM torus initially between $20 r_g$ and $100 r_g$ around a black hole with $a = 0$. Left: history of accretion rate around the horizon and outflow rate. The black line is the best-fit model of accretion rate in Metzger et al. (2008) and the gray lines are the scatter. The accretion rate decreases with time following $\dot{M} \propto t^{-2}$ when $t \gg t_{visc,0}$. Right: Bound mass, accreted mass, and unbound mass as a function of time.

in Section 3.5 with $r_{in} = 20 r_g$, $r_{out} = 100 r_g$ and spin $a = 0$. After $10^6 t_g$, as the torus expands to a larger scale, we increase the number of levels from $n = 6$ to $n = 8$ to further speed up the simulation. Then after $3 \times 10^6 t_g$, we again increase n to $n = 10$ and evolve it to $10^7 t_g$.

Figure 14 shows the long-term evolution of the torus accretion including the evolution of mass and accretion rate. We separate the mass into bound ($\mathcal{B}_{gas} < 0$) and unbound ($\mathcal{B}_{gas} > 0$) using the hydrodynamic Bernoulli parameter

$$\mathcal{B}_{gas} = -u_t(\rho + u + p)/\rho - 1. \quad (26)$$

As shown in Figure 14, $\sim 40\%$ of the mass of the torus is accreted while the rest is turned into outflow that escapes to infinity. The accretion rate gradually decreases from ~ 1 to $\sim 10^{-4}$.

The secular evolution of an accretion flow with fixed scale height h/r , conserved total angular momentum, and no outflows follows $\dot{M} \propto t^{-4/3}$. Metzger et al. (2008) provides a series of solutions considering mass and angular momentum loss. The outflow is parameterized using

$$\dot{M}_{out} = \left[1 - \left(\frac{r_*}{r_d}\right)^p\right] \frac{f M_d}{t_{visc}}, \quad (27)$$

where r_* is the radius of the no-torque boundary condition, r_d is radius of the disk, M_d is the disk mass, and

t_{visc} is the viscous time. The angular momentum loss rate from the disk is

$$\dot{J} = -C \dot{M}_{out} (G M r_d)^{1/2}, \quad (28)$$

where C is a constant that depends on the torque exerted by the outflowing mass on the remaining disk. For $C(r_*/r_d)^p \ll 1 - C$, the disk mass evolves as

$$M_d \simeq M_{d,0} \left[1 + 3f(1 - C) \left(\frac{t}{t_{visc,0}}\right)\right]^{-1/[3(1-C)]}, \quad (29)$$

and the accretion rate follows

$$\begin{aligned} \dot{M}_{acc} \simeq & f \frac{M_{d,0}}{t_{visc,0}} \left(\frac{r_*}{r_{d,0}}\right)^p \\ & \times \left[1 + 3f(1 - C) \left(\frac{t}{t_{visc,0}}\right)\right]^{-\frac{1}{3(1-C)} - 1 - \frac{2p}{3}}. \end{aligned} \quad (30)$$

We use $f = 1.6$ following Metzger et al. (2008), and fix $r_* = 6 r_g$ and $r_{d,0} = 50 r_g$.

Using the formula in Metzger et al. (2008), we fit the evolution of disk mass and accretion rate respectively. We only fit for $10^4 < t/t_g < 4 \times 10^6$ since the MRI is not fully developed at early times and the gas is too loosely bounded to be thought of a disk at late times. For evolution of the accretion rate, we find $t_{visc,0} = 1.10^{+0.28}_{-0.25} \times 10^5 t_g$, $C = 0.56^{+0.06}_{-0.07}$, and $p = 0.44^{+0.04}_{-0.04}$. For evolution of disk mass, we use

the bound mass as a proxy of the disk mass and find $t_{\text{visc},0} = 1.70_{-0.40}^{0.46} \times 10^5 t_g$ and $C = 0.59_{-0.06}^{0.05}$. The fits are overplotted in Figure 14. These two fits are consistent with each other, implying a result of $C \approx 1/2$ and $p \approx 1/2$. Note also that $t_{\text{visc},0} \sim 10^5 t_g$ corresponds to $t_{\text{visc},0} \sim 300 r_{\text{d},0}^{3/2}$ which is consistent with $h/r \sim 1/3$ and a dimensionless stress $\alpha \sim 0.03$. The fits found here correspond to a late-time evolution of the bound disk mass and accretion rate scaling as $M_{\text{disk}} \propto t^{-2/3}$ and $\dot{M}_{\text{in}} \propto t^{-2}$. We will analyze additional details of this evolution in future work.

5. DISCUSSION

The tests presented above demonstrate that the cyclic zoom method is able to connect large scales and small scales for various problems and different initial conditions related to gas flows around compact objects. It is able to pass the information from small scales to large scales and vice versa, preserving predictions for mass and energy fluxes in accretion problems. Below we discuss the limitations, advantages, comparisons to previous work, and future applications of this technique.

5.1. Difficulties and Limitations

Given the turbulent nature of the accretion flow, there are intrinsic difficulties in comparing standard runs and the cyclic zoom runs at the “same” time. Even for standard simulations, the details of a numerical solution can be different if we compute it again when the fluid is turbulent, because the chaotic non-linear dynamics can amplify tiny differences originating in small variations in floating point roundoff. That is why we compare statistical properties, such as averaged values and their dispersion, in most cases.

Our method effectively “freezes” the small-scale physics to control the accretion onto small scales and power the feedback to larger scales. This means that the short-time variability of the real physical system may not be sufficiently captured. More frequent sampling, or different strategies for carrying out the cyclic zoom, like “F” or “W” patterns in the space-time domain, may help to capture more of the small-scale variability. In addition, the evolution of the mask region can be made more sophisticated to capture more of the small-scale information. For example, instead of using the variables right before the mesh refinement, one may use the time-averaged variables or a more data-driven model. There might also be some room for investigating the optimal size of the mask region in higher-resolution simulations.

5.2. Speedup

Figure 1 illustrates the speedup that can be obtained with the cyclic zoom method. For a normal GRMHD

simulation using AMR or spherical coordinates, the computation time, t_{comp} , scales with the characteristic length scale of interest, r_{char} , as $t_{\text{comp}} \propto r_{\text{char}}^{3/2}$. The characteristic time varies as $t_{\text{char}} \propto r_{\text{char}}^{3/2}$, where the characteristic speed scales as $v_{\text{char}} \propto r_{\text{char}}^{-1/2}$. Using the cyclic zoom method, we can ideally achieve $t_{\text{comp}} \propto \log r_{\text{char}}$ and thus a speedup of $\propto r_{\text{char}}^{3/2}$ since the simulation spends a similar amount of time on all scales in terms of characteristic timescale.

However, in the presence of material with realistic speed on large scales, e.g., jets due to a spinning black hole, we have $t_{\text{comp}} \propto r_{\text{char}}^{1/2}$ using cyclic zoom and thus a speedup $\propto r_{\text{char}}$. Therefore, the actual computation time can typically be expected to lie between these two limits, i.e., $t_{\text{comp}} \propto r_{\text{char}}^{0-0.5}$, and thus a realistic speedup is $\propto r_{\text{char}}^{1-1.5}$, as shown by the cyclic zoom runs in Figure 1. In addition, since we typically spend more time when $i = 0$, the scaling of the cyclic zoom method has a relatively large coefficient in front due to the corresponding overhead. Depending on how many levels we are using for the cyclic zoom, and how much time we spend on each level, the speedup can be higher or lower by factors of a few. Given the computational resources available, we can flexibly choose how much high-frequency information we want to obtain, as long as we keep $r_{\text{z,max}} \lesssim r_{\text{char}}$ and $t_{\text{run,max}} \lesssim t_{\text{char}}$. Overall we can achieve a speedup of $\gtrsim 10^5$ for galactic scale simulations. Note that this allows simulations that would take more than hundreds of years to run to be effectively completed within a few days or weeks.

5.3. Comparison to previous work

The work presented here was inspired by Cho et al. (2023) that presented a “multi-zone” method for bridging scales and tested it for Bondi accretion. They successfully spanned 7 orders of magnitude in radius and simulated accretion onto a non-spinning SMBH from an external medium with a Bondi radius $\gtrsim 10^5 r_g$. Cho et al. (2024) further applied the method to simulations using initial conditions from a large-scale galaxy simulation and achieved a steady state over 8 decades in radius. Our method preserves the spirit of “V-cycle” or “Λ-cycle” as in their method.

However, we treat the magnetic field in a different manner. We still evolve the magnetic field \mathbf{B} in the mask region while Cho et al. (2024) holds the magnetic field fixed when the zone is not active. In this way, our method can avoid the strong shear of the magnetic field around the boundary when there is rotation and inhomogeneity. The shear of the magnetic field may not be severe when the flow is uniform or mainly radial. However, in the presence of a rotating disk or a spinning

black hole powering a jet, it could be a significant issue. To both evolve the magnetic field and avoid the severe timestep constraint, we opt for nested mesh with AMR instead of using a set of spherical annuli as in [Cho et al. \(2023, 2024\)](#). These key differences help us to handle a range of applications involving strong magnetic field or rotation (e.g., torus accretion; see Section 3.4).

For the magnetized Bondi accretion onto a nonspinning black hole over galactic scales, we find a very similar accretion rate and feedback power as [Cho et al. \(2023\)](#) and [Cho et al. \(2024\)](#), providing strong validation of both methods for this problem.

5.4. Future Applications

The cyclic zoom method opens a window for various applications in the future to address increasingly realistic and complex problems. Of particular interest are investigations of Bondi accretion and torus accretion onto SMBHs coupled to galactic scales. In the presence of gas cooling and a large-scale gravitational potential from a galaxy, we can apply this method to multi-phase accretion from galactic scales but using ab-initio calculations instead of ad-hoc models in current simulation (e.g., [Fournier et al. 2024](#); [Grete et al. 2025](#)). More realistically, we could use this method to perform simulations using galaxies from cosmological simulations like the IllustrisTNG project ([Pillepich et al. 2018](#); [Springel et al. 2018](#)) instead of using current analytic or semi-analytic models for accretion and feedback (e.g., [Weinberger et al. 2017, 2025](#)). In addition, the method can probably be generalized to GR-radiation MHD ([White et al. 2023](#); [Stone et al. 2024](#)) and/or non-ideal GRMHD ([Ripperda et al. 2019](#)). In both cases, quantitative comparisons to fully resolved simulations to test the method will be necessary. More broadly, the method holds a lot of promise for being applied to many other problems where there are vast spatial and temporal scales to cover, e.g., convection in stars.

6. SUMMARY

In this work, we have introduced the cyclic zoom method to resolve the dynamics of the accretion flow onto a black hole over a vast range of spatial and temporal scales in 3D GRMHD simulations. In this approach, we cyclically zoom out (derefine) and zoom in (refine) the simulation domain with a mask region in the center to preserve the small-scale physics and mediate an information flow from small to large scales and vice versa. The method can accelerate the GRMHD simulations by more than a factor of $\sim 10^5$.

We establish the validity of the method using a series of test problems including spherically symmetric Bondi

accretion, monopole spin down of a rotating black hole, magnetized turbulent Bondi accretion, torus accretion, and long-term secular evolution of a torus around both Schwarzschild and Kerr black holes. As applications, we simulate Bondi accretion and torus accretion of black holes from galactic scales onto both non-spinning and spinning black holes. For Bondi accretion, we find that the density scales with radius as $\rho \propto r^{-1}$ inside the Bondi radius. The accretion rate is suppressed relative to the Bondi rate by $\sim (10r_g/r_B)^{1/2}$. We find energy feedback to the Bondi scale with a flux of $\sim 0.01\dot{M}c^2$ for spin $a = 0$, and $0.1\dot{M}c^2$ for $a \approx 0.9$. For accretion of a torus, our model is able to capture the correct feedback efficiency and long-term secular evolution. We find that the accretion rate of a torus decreases with time as $\dot{M} \propto t^{-2}$ when the timescale is much longer than the viscous timescale.

By connecting physics at various scales, our approach aims to bridge the gap between galaxy scales and the event horizon of black holes. This method may lead to a more comprehensive sub-grid model of black hole growth and feedback in large-scale galaxy formation cosmological simulations. The technique can furthermore be generalized to many other problems where there is a vast range of spatial and temporal scales to cover.

ACKNOWLEDGMENTS

We thank Hyerin Cho, Ramesh Narayan, Alexander Tchekhovskoy, and Chang-Goo Kim for many useful conversations. We thank the anonymous referee for the helpful comments and suggestions. This work was supported by a grant from the Simons Foundation (888968, E.C. Ostriker, Princeton University PI) as part of the Learning the Universe Collaboration. J.S. acknowledges support from the Eric and Wendy Schmidt Fund for Strategic Innovation. E.Q. was supported in part by a Simons Investigator grant from the Simons Foundation and NSF AST grant 2107872. We acknowledge the EuroHPC Joint Undertaking for awarding this project access to the EuroHPC supercomputer LUMI, hosted by CSC (Finland) and the LUMI consortium through a EuroHPC Regular Access call. The authors are pleased to acknowledge that the work reported on in this paper was substantially performed using the Princeton Research Computing resources at Princeton University, which is consortium of groups led by the Princeton Institute for Computational Science and Engineering (PICSciE) and Office of Information Technology's Research Computing. This work used the Delta system at the National Center for Supercomputing Applications through allocation PHY230165 from the Advanced Cyberinfrastructure Coordination Ecosystem: Services &

Support (ACCESS) program, which is supported by National Science Foundation grants #2138259, #2138286,

#2138307, #2137603, and #2138296 (Boerner et al. 2023).

Software: AthenaK (Stone et al. 2024)

APPENDIX

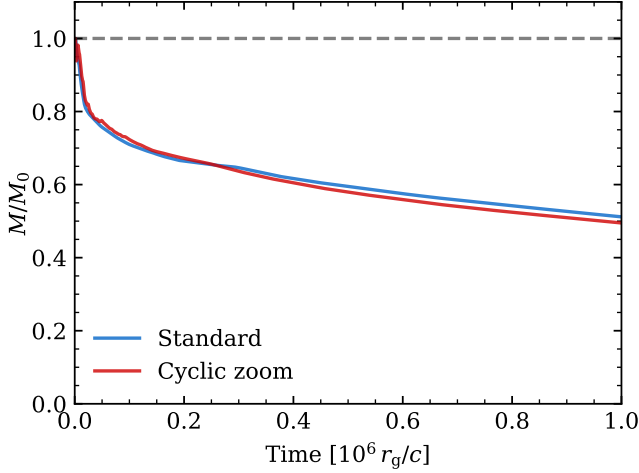


Figure 15. History of the total mass in the simulation domain of the standard run and the cyclic zoom run of the long-term evolution of torus accretion with $a = 0$. The relative difference is $\lesssim 1\%$.

A. CONSERVATION OF MASS

As we mentioned in Section 2, the cyclic zoom method is no longer conservative to machine precision since the

hydrodynamic variables are not evolved in the mask region (note, however, that magnetic flux is conserved since we evolve magnetic fields inside the mask). In order to assess how significant the lack of conservation is, Figure 15 shows the mass history for the long-term accretion of a rotating torus around a non-spinning black hole presented in Section 3.5. At the end of the simulation ($t = 10^6 t_g$), 50% of the initial mass is left in the simulation domain with 40% accreted and 10% escaping the outer boundary (see also Figure 14). The relative difference of mass remaining in the domain is $\lesssim 1\%$. Note that this is not an actual measure of the mass lost or gained in the cyclic zoom model but rather just the difference between the evolution of the two models (which as we argue in Section 5.1 is always expected). Instead, the figure shows that the amount of mass lost or gained in the cyclic zoom model is negligible compared to the overall mass evolution of the torus due to dynamics.

REFERENCES

- Anglés-Alcázar, D., Quataert, E., Hopkins, P. F., et al. 2021, *ApJ*, 917, 53, doi: [10.3847/1538-4357/ac09e8](https://doi.org/10.3847/1538-4357/ac09e8)
- Blandford, R. D., & Znajek, R. L. 1977, *MNRAS*, 179, 433, doi: [10.1093/mnras/179.3.433](https://doi.org/10.1093/mnras/179.3.433)
- Boerner, T. J., Deems, S., Furlani, T. R., Knuth, S. L., & Towns, J. 2023, in *Practice and Experience in Advanced Research Computing, PEARC '23* (New York, NY, USA: Association for Computing Machinery), 173–176, doi: [10.1145/3569951.3597559](https://doi.org/10.1145/3569951.3597559)
- Bondi, H. 1952, *MNRAS*, 112, 195, doi: [10.1093/mnras/112.2.195](https://doi.org/10.1093/mnras/112.2.195)
- Chael, A. 2024, *MNRAS*, 532, 3198, doi: [10.1093/mnras/stae1692](https://doi.org/10.1093/mnras/stae1692)
- . 2025, *MNRAS*, 537, 2496, doi: [10.1093/mnras/staf200](https://doi.org/10.1093/mnras/staf200)
- Cho, H., Prather, B. S., Narayan, R., et al. 2023, *ApJL*, 959, L22, doi: [10.3847/2041-8213/ad1048](https://doi.org/10.3847/2041-8213/ad1048)
- Cho, H., Prather, B. S., Su, K.-Y., Narayan, R., & Natarajan, P. 2024, *ApJ*, 977, 200, doi: [10.3847/1538-4357/ad9561](https://doi.org/10.3847/1538-4357/ad9561)
- Event Horizon Telescope Collaboration, Akiyama, K., Alberdi, A., et al. 2019, *ApJL*, 875, L1, doi: [10.3847/2041-8213/ab0ec7](https://doi.org/10.3847/2041-8213/ab0ec7)
- Ferrarese, L., & Merritt, D. 2000, *ApJL*, 539, L9, doi: [10.1086/312838](https://doi.org/10.1086/312838)
- Fishbone, L. G., & Moncrief, V. 1976, *ApJ*, 207, 962, doi: [10.1086/154565](https://doi.org/10.1086/154565)
- Fournier, M., Grete, P., Brüggén, M., Glines, F. W., & O’Shea, B. W. 2024, *A&A*, 691, A239, doi: [10.1051/0004-6361/202451031](https://doi.org/10.1051/0004-6361/202451031)
- Galishnikova, A., Philippov, A., Quataert, E., Chatterjee, K., & Liska, M. 2025, *ApJ*, 978, 148, doi: [10.3847/1538-4357/ad9926](https://doi.org/10.3847/1538-4357/ad9926)

- Gammie, C. F., McKinney, J. C., & Tóth, G. 2003, *ApJ*, 589, 444, doi: [10.1086/374594](https://doi.org/10.1086/374594)
- Gaspari, M., Tombesi, F., & Cappi, M. 2020, *Nature Astronomy*, 4, 10, doi: [10.1038/s41550-019-0970-1](https://doi.org/10.1038/s41550-019-0970-1)
- Gebhardt, K., Bender, R., Bower, G., et al. 2000, *ApJL*, 539, L13, doi: [10.1086/312840](https://doi.org/10.1086/312840)
- Grete, P., O’Shea, B. W., Glines, F. W., et al. 2025, *arXiv e-prints*, arXiv:2502.13213, <https://arxiv.org/abs/2502.13213>
- Guo, M., Inayoshi, K., Michiyama, T., & Ho, L. C. 2020, *ApJ*, 901, 39, doi: [10.3847/1538-4357/abacc1](https://doi.org/10.3847/1538-4357/abacc1)
- Guo, M., Stone, J. M., Kim, C.-G., & Quataert, E. 2023, *ApJ*, 946, 26, doi: [10.3847/1538-4357/acb81e](https://doi.org/10.3847/1538-4357/acb81e)
- Guo, M., Stone, J. M., Quataert, E., & Kim, C.-G. 2024, *ApJ*, 973, 141, doi: [10.3847/1538-4357/ad5fe7](https://doi.org/10.3847/1538-4357/ad5fe7)
- Hawley, J. F., Smarr, L. L., & Wilson, J. R. 1984, *ApJ*, 277, 296, doi: [10.1086/161696](https://doi.org/10.1086/161696)
- Hopkins, P. F., & Quataert, E. 2010, *MNRAS*, 407, 1529, doi: [10.1111/j.1365-2966.2010.17064.x](https://doi.org/10.1111/j.1365-2966.2010.17064.x)
- . 2011, *MNRAS*, 415, 1027, doi: [10.1111/j.1365-2966.2011.18542.x](https://doi.org/10.1111/j.1365-2966.2011.18542.x)
- Hopkins, P. F., Grudic, M. Y., Su, K.-Y., et al. 2024a, *The Open Journal of Astrophysics*, 7, 18, doi: [10.21105/astro.2309.13115](https://doi.org/10.21105/astro.2309.13115)
- Hopkins, P. F., Squire, J., Su, K.-Y., et al. 2024b, *The Open Journal of Astrophysics*, 7, 19, doi: [10.21105/astro.2310.04506](https://doi.org/10.21105/astro.2310.04506)
- Hopkins, P. F., Su, K.-Y., Murray, N., et al. 2025, *arXiv e-prints*, arXiv:2502.05268, doi: [10.48550/arXiv.2502.05268](https://doi.org/10.48550/arXiv.2502.05268)
- Kaaz, N., Liska, M., Tchekhovskoy, A., Hopkins, P. F., & Jacquemin-Ide, J. 2025, *ApJ*, 979, 248, doi: [10.3847/1538-4357/ad9a86](https://doi.org/10.3847/1538-4357/ad9a86)
- Kaaz, N., Murguia-Berthier, A., Chatterjee, K., Liska, M. T. P., & Tchekhovskoy, A. 2023, *ApJ*, 950, 31, doi: [10.3847/1538-4357/acc7a1](https://doi.org/10.3847/1538-4357/acc7a1)
- Kormendy, J., & Ho, L. C. 2013, *ARA&A*, 51, 511, doi: [10.1146/annurev-astro-082708-101811](https://doi.org/10.1146/annurev-astro-082708-101811)
- Koudmani, S., Somerville, R. S., Sijacki, D., et al. 2024, *MNRAS*, 532, 60, doi: [10.1093/mnras/stae1422](https://doi.org/10.1093/mnras/stae1422)
- Kozłowski, M., Jaroszynski, M., & Abramowicz, M. A. 1978, *A&A*, 63, 209
- Lalakos, A., Tchekhovskoy, A., Bromberg, O., et al. 2024, *ApJ*, 964, 79, doi: [10.3847/1538-4357/ad0974](https://doi.org/10.3847/1538-4357/ad0974)
- Lalakos, A., Gottlieb, O., Kaaz, N., et al. 2022, *ApJL*, 936, L5, doi: [10.3847/2041-8213/ac7bed](https://doi.org/10.3847/2041-8213/ac7bed)
- Lemaster, M. N., & Stone, J. M. 2009, *ApJ*, 691, 1092, doi: [10.1088/0004-637X/691/2/1092](https://doi.org/10.1088/0004-637X/691/2/1092)
- Li, Y., & Bryan, G. L. 2014, *ApJ*, 789, 153, doi: [10.1088/0004-637X/789/2/153](https://doi.org/10.1088/0004-637X/789/2/153)
- Magorrian, J., Tremaine, S., Richstone, D., et al. 1998, *AJ*, 115, 2285, doi: [10.1086/300353](https://doi.org/10.1086/300353)
- Metzger, B. D., Piro, A. L., & Quataert, E. 2008, *MNRAS*, 390, 781, doi: [10.1111/j.1365-2966.2008.13789.x](https://doi.org/10.1111/j.1365-2966.2008.13789.x)
- Michel, F. C. 1972, *Ap&SS*, 15, 153, doi: [10.1007/BF00649949](https://doi.org/10.1007/BF00649949)
- Narayan, R., Chael, A., Chatterjee, K., Ricarte, A., & Curd, B. 2022, *MNRAS*, 511, 3795, doi: [10.1093/mnras/stac285](https://doi.org/10.1093/mnras/stac285)
- Narayan, R., Sądowski, A., Penna, R. F., & Kulkarni, A. K. 2012, *MNRAS*, 426, 3241, doi: [10.1111/j.1365-2966.2012.22002.x](https://doi.org/10.1111/j.1365-2966.2012.22002.x)
- Ni, Y., Chen, N., Zhou, Y., et al. 2024, *arXiv e-prints*, arXiv:2409.10666, doi: [10.48550/arXiv.2409.10666](https://doi.org/10.48550/arXiv.2409.10666)
- Ni, Y., Di Matteo, T., Bird, S., et al. 2022, *MNRAS*, 513, 670, doi: [10.1093/mnras/stac351](https://doi.org/10.1093/mnras/stac351)
- Olivares, H. R., Mościbrodzka, M. A., & Porth, O. 2023, *A&A*, 678, A141, doi: [10.1051/0004-6361/202346010](https://doi.org/10.1051/0004-6361/202346010)
- Pillepich, A., Springel, V., Nelson, D., et al. 2018, *MNRAS*, 473, 4077, doi: [10.1093/mnras/stx2656](https://doi.org/10.1093/mnras/stx2656)
- Porth, O., Chatterjee, K., Narayan, R., et al. 2019, *ApJS*, 243, 26, doi: [10.3847/1538-4365/ab29fd](https://doi.org/10.3847/1538-4365/ab29fd)
- Ressler, S. M., Quataert, E., & Stone, J. M. 2018, *MNRAS*, 478, 3544, doi: [10.1093/mnras/sty1146](https://doi.org/10.1093/mnras/sty1146)
- Ressler, S. M., White, C. J., Quataert, E., & Stone, J. M. 2020, *ApJL*, 896, L6, doi: [10.3847/2041-8213/ab9532](https://doi.org/10.3847/2041-8213/ab9532)
- Ripperda, B., Bacchini, F., Porth, O., et al. 2019, *ApJS*, 244, 10, doi: [10.3847/1538-4365/ab3922](https://doi.org/10.3847/1538-4365/ab3922)
- Russell, H. R., Fabian, A. C., McNamara, B. R., & Broderick, A. E. 2015, *MNRAS*, 451, 588, doi: [10.1093/mnras/stv954](https://doi.org/10.1093/mnras/stv954)
- Springel, V., Pakmor, R., Pillepich, A., et al. 2018, *MNRAS*, 475, 676, doi: [10.1093/mnras/stx3304](https://doi.org/10.1093/mnras/stx3304)
- Stone, J. M., Tomida, K., White, C. J., & Felker, K. G. 2020, *ApJS*, 249, 4, doi: [10.3847/1538-4365/ab929b](https://doi.org/10.3847/1538-4365/ab929b)
- Stone, J. M., Mullen, P. D., Fielding, D., et al. 2024, *arXiv e-prints*, arXiv:2409.16053, doi: [10.48550/arXiv.2409.16053](https://doi.org/10.48550/arXiv.2409.16053)
- Su, K.-Y., Bryan, G. L., Haiman, Z., et al. 2023, *MNRAS*, 520, 4258, doi: [10.1093/mnras/stad252](https://doi.org/10.1093/mnras/stad252)
- Tchekhovskoy, A., Narayan, R., & McKinney, J. C. 2011, *MNRAS*, 418, L79, doi: [10.1111/j.1745-3933.2011.01147.x](https://doi.org/10.1111/j.1745-3933.2011.01147.x)
- Tremmel, M., Karcher, M., Governato, F., et al. 2017, *MNRAS*, 470, 1121, doi: [10.1093/mnras/stx1160](https://doi.org/10.1093/mnras/stx1160)
- Weinberger, R., Bhowmick, A., Blecha, L., et al. 2025, *arXiv e-prints*, arXiv:2502.13241, <https://arxiv.org/abs/2502.13241>
- Weinberger, R., Springel, V., Hernquist, L., et al. 2017, *MNRAS*, 465, 3291, doi: [10.1093/mnras/stw2944](https://doi.org/10.1093/mnras/stw2944)

- White, C. J., Mullen, P. D., Jiang, Y.-F., et al. 2023, ApJ, 949, 103, doi: [10.3847/1538-4357/acc8cf](https://doi.org/10.3847/1538-4357/acc8cf)
- White, C. J., Quataert, E., & Gammie, C. F. 2020, ApJ, 891, 63, doi: [10.3847/1538-4357/ab718e](https://doi.org/10.3847/1538-4357/ab718e)
- White, C. J., Stone, J. M., & Gammie, C. F. 2016, ApJS, 225, 22, doi: [10.3847/0067-0049/225/2/22](https://doi.org/10.3847/0067-0049/225/2/22)
- Xu, W. 2023, ApJ, 954, 180, doi: [10.3847/1538-4357/ace892](https://doi.org/10.3847/1538-4357/ace892)
- Xu, W., & Stone, J. M. 2019, MNRAS, 488, 5162, doi: [10.1093/mnras/stz2002](https://doi.org/10.1093/mnras/stz2002)
- Yang, H., Yuan, F., Yuan, Y.-F., & White, C. J. 2021, ApJ, 914, 131, doi: [10.3847/1538-4357/abfe63](https://doi.org/10.3847/1538-4357/abfe63)
- Yuan, F., & Narayan, R. 2014, ARA&A, 52, 529, doi: [10.1146/annurev-astro-082812-141003](https://doi.org/10.1146/annurev-astro-082812-141003)